Nonlinear Dyn (2023) 111:22215–22236
https://doi.org/10.1007/s11071-023-08888-8

ORIGINAL PAPER

Simultaneous passive suppression and energy harvesting from galloping using a bistable piezoelectric nonlinear energy sink

Guilherme Rosa Franzini ·
Vitor Schwenck Franco Maciel ·
Guilherme Jorge Vernizzi · **Daniele Zulli**

Received: 30 March 2023 / Accepted: 28 August 2023 / Published online: 21 September 2023

Abstract The paper brings analytical–numerical studies on the problem of simultaneous passive suppression of the galloping of a square prism and energy harvesting. For this, a device named bistable piezoelectric nonlinear energy sink (BSPNES), defined as a small mass linked to the main structure by a piezoelectric pre-compressed spring and a linear dashpot, is employed. The focus is the comparison of the BSPNES performance with that obtained from its monostable counterpart. The numerical results show that the BSPNES performs better than its monostable counterpart for practically the whole range of reduced velocities. More specifically, for a certain range of reduced velocities, both the suppression efficiency and the harvested energy achieved by the BSPNES are significantly larger than those from its monostable counterpart. Besides the numerical results, a perturbation method, proper for strong nonlinearities, is applied. The results from this perturbation method very well agree with those from the numerical integration of the mathematical model.

Keywords Passive suppression · Energy harvesting · Galloping · Piezoelectric nonlinear energy sink

List of symbols

M, L	Prism mass and length, respectively
D	Side of the cross section
k_y, c_y	Stiffness and damping constant of the support, respectively
m_N, c_N, k	Suppressor mass, damping and spring constants, respectively
ρ	Fluid specific mass
U_∞	Free stream velocity
Y	Dimensional prism displacement
W	Dimensional suppressor displacement
V	Dimensional electric tension
R, C_P	Resistance and capacitance, respectively
θ	Electro-mechanical coupling term
ℓ_0	Neutral length of the suppressor spring
ℓ_1	Length of the suppressor spring at $W = 0$
$\omega = \sqrt{\frac{k_y}{M+m_N}}$	Reference frequency
$V_0 = \frac{m_N \omega^2 \ell_1}{2\theta}$	Reference electric tension

G. R. Franzini (✉) · V. S. F. Maciel · G. J. Vernizzi
Offshore Mechanics Laboratory, Escola Politécnica, University of São Paulo, São Paulo, SP, Brazil
e-mail: gfranzini@usp.br

V. S. F. Maciel
e-mail: vitor.maciel@usp.br

G. J. Vernizzi
e-mail: guilherme.jorge.lopes@usp.br

D. Zulli
Department of Civil, Construction-Architectural and Environmental Engineering, University of L'Aquila, L'Aquila, AQ, Italy
e-mail: daniele.zulli@univaq.it

A_n $(n = 1, \ldots, 7)$	Aerodynamic coefficients
C_y	Cross-wise force coefficient
$m^* = \frac{m_N+M}{\rho D^2 L}$	Dimensionless mass
$\hat{m} = \frac{m_N}{m_N+M}$	Dimensionless suppressor mass
$U_r = \frac{U_\infty}{\omega D}$	Reduced velocity
U_r^c	Critical reduced velocity
U_0	Critical reduced velocity for the Pure Galloping case
$\zeta_y = \frac{c_y}{2(M+m_N)\omega}$	Prism damping ratio
$\zeta_N = \frac{c_N}{2m_N\omega}$	Suppressor damping ratio
$\tau = \omega t$	Dimensionless time
$y = \frac{Y}{D}$	Dimensionless prism displacement
$w = \frac{W}{\ell_1}$	Dimensionless suppressor displacement
$v = \frac{V}{V_0}$	Dimensionless electric tension
$\hat{y}$	Characteristic dimensionless oscillation amplitude of the prism
$\hat{y}_0$	Characteristic dimensionless oscillation amplitude of the prism under Pure Galloping

1 Introduction

Galloping is a particular flow-induced vibration (FIV) phenomenon characterized by oscillatory responses that appear when the free stream velocity is larger than the critical value associated with the Hopf bifurcation. Differently from vortex-induced vibrations (VIV), the oscillations due to galloping monotonically increase with the increase in the free stream velocity. Further details regarding galloping can be found in the classical textbooks [1–3].

The occurrence of vibrations is usually unwanted, especially when the structures are subjected to long operational life cycles and are thus susceptible to fatigue damage. Consequently, several solutions for the passive suppression of oscillations have been studied in the literature. A classical and well established solution is the tuned mass damper (TMD), which consists of a mass (or set of masses) linked to the main structure by linear springs and dashpots. For further discussions regarding the use of TMDs, see [4].

Properly tuned TMDs have been shown to be very efficient when the external excitation is narrow-banded. However, if a broad-banded external excitation is considered instead, marked reductions on the efficiency of the suppressor may be observed. Additionally, due to their tuning nature, the robustness of the suppression achieved can also be questioned due to other environmental factors [5]. These limitations have motivated the study of the so-called nonlinear energy sinks (NESs). Following the definitions presented in [5], a NES is a substructure coupled to the main structure by means of a (usually) linear dashpot such that the device has no linear natural frequency (essentially nonlinear character). Under these conditions, energy is transferred from the main structure to the suppressor, in which it is dissipated. This mechanism of energy transfer and dissipation is named energy pumping or Targeted Energy Transfer (TET). References [6–8] discuss the TET mechanism in greater depth.

Several studies have recently addressed the use of NESs as passive suppressors for different FIV phenomena, including VIV [9–18]), galloping [19–24], other aeroelastic phenomena [25,26] and vibrations induced by the internal flow [27–29]. Additional applications of NESs to different engineering problems are discussed in [30,31].

Different concepts of NESs can be found in the literature, including the rotational one [32,33] and those based on vibro-impact (see, for example, [34–36]). The focus herein lies on the bistable NES (BSNES). Among the different strategies for obtaining a BSNES, we highlight the one described in [37], which uses pre-compressed springs placed orthogonally to the direction of the suppressor displacements. Other applications of BSNESs as passive suppressors can be found in [38–40].

Energy harvesting from structural vibrations has also received increased focus in the past decades. Among other forms of electro-mechanical energy conversion, this paper focuses on the piezoelectric one. A piezoelectric material is one in which a mechanical stress causes both mechanical strain and electric tension (direct effect). In addition, the application of electric tension to a piezoelectric material leads to mechanical strain (inverse effect). Erturk and Inman [41] brings comprehensive discussions regarding piezoelectric energy harvesting. Due to their self-excited character, FIV problems are potential sources of vibration for energy harvesting solutions and have been the focus of several recent papers (see, for example, [42–51]). Abdelkefi [52] brings a literature review on energy harvesting from aeroelastic phenomena while [53] discusses perspectives of energy harvesting from FIV.

Note that energy harvesting from FIV can be useful for charging low-power equipment, such as small sensors.

Two other important aspects on the topic of energy harvesting are now discussed. The first is the inclusion of nonlinearities as a way to enhance the energy harvesting efficiency. Paula et al. [54], for example, shows that the piezoelectric energy harvesting from the vibrations of a cantilevered beam is more efficient if nonlinearities associated with the placement of magnets are considered in the experimental arrangement. The second aspect worth mentioning is related to recent studies which focus on taking advantage of the dynamic responses of NESs for energy harvesting purposes. In the latter scenario, examples of devices for the combined energy harvesting and passive suppression include a magnet fixed to an oscillating beam close to other two externally placed magnets [55] and the VIV of cylinder fitted with a rotational NES linked to an ideal generator; see [56].

In this paper, we present numerical and analytical studies for a solution to simultaneously alleviate the response of a rigid and elastically mounted square prism to the galloping phenomenon and perform electro-mechanical energy conversion by the piezoelectric effect. The device used for this purpose is composed of a mass linked to the main structure by a linear dashpot and a pre-compressed piezoelectric spring. Since the springs are pre-compressed, the system has two stable equilibrium points, leading to a solution herein named bistable piezoelectric nonlinear energy sink (BSPNES). To the best of the authors' knowledge, such a device for the combined problem has not been addressed in the literature, which provides novelty to the present work. The rest of the paper is structured as follows. Section 2 describes the mathematical model. Next, Sect. 3 details the analysis methodologies and the results are discussed in Sect. 4. The conclusions are addressed in Sect. 5 and Appendix A brings a discussion on bistability on a simpler, albeit representative problem.

2 Mathematical model

The governing equations are obtained by the Euler-Lagrange formalism. In this approach, we define Y as the displacement of the prism, W as the displacement of the suppressor with respect to the prism and V as the electric tension at the energy harvesting circuit. A square of side D defines the cross-section of the prism, which has mass M and length L. The prism is mounted on an elastic support characterized by linear stiffness k_y and damping constant c_y. The free stream velocity is considered uniform and given by U_∞. The support allows for displacements only in the cross-wise direction (direction orthogonal to the free stream velocity) and the surrounding fluid has specific mass ρ. Figure 1 sketches the problem investigated.

The device for simultaneous suppression and energy harvesting has mass m_N and is connected to the prism using a pre-compressed piezoelectric spring of stiffness k and capacitance C_P. The essentially nonlinear dynamics of the suppressor is achieved by considering that the spring is orthogonal to the direction of the motion of the device when $W = 0$. The energy harvesting circuit is composed of an electric load R and the neutral (unloaded) length of the piezoelectric spring is ℓ_0. As depicted in Fig. 1, the stretched length of the piezoelectric spring is $\ell = \sqrt{\ell_1^2 + W^2}$. The assemblage of the device to the prism does not allow impacts between these elements.

The constitutive equation of the piezoelectric spring is given by Eqs. 1 and 2 [57].

$$F_{el} = k\Delta\ell - \theta V \tag{1}$$

$$Q = \theta\Delta\ell + C_P V \tag{2}$$

where F_{el} is the spring force, $\Delta\ell = \ell - \ell_0$ is the variation of the length of the piezoelectric spring, Q is the electric charge and θ is the electro-mechanical coupling term. Notice that the constitutive equations are linear in both $\Delta\ell$ and V. However, since $\Delta\ell$ depends on W in a nonlinear form, the resulting equations of motion present nonlinear terms due to the piezoelectric spring.

Kinetic energy $\mathcal{T}$, elastic potential energy $\mathcal{U}$ and electric internal energy $\mathcal{W}$ read:

$$\mathcal{T} = \frac{1}{2}M(Y')^2 + \frac{1}{2}m_N(Y' + W')^2 \tag{3}$$

$$\begin{aligned}\mathcal{U} &= \frac{1}{2}k_y Y^2 + \int F_{el} d\Delta\ell \\ &= \frac{1}{2}k_y Y^2 + \frac{1}{2}k(\Delta\ell)^2 - \theta\Delta\ell V\end{aligned} \tag{4}$$

$$\mathcal{W} = \int Q dV = \theta\Delta\ell V + \frac{1}{2}C_P V^2 \tag{5}$$

$(\,)'$ being the derivative with respect to time.

Fig. 1 Schematic representation. The gravitational acceleration is in the direction of the prism axis

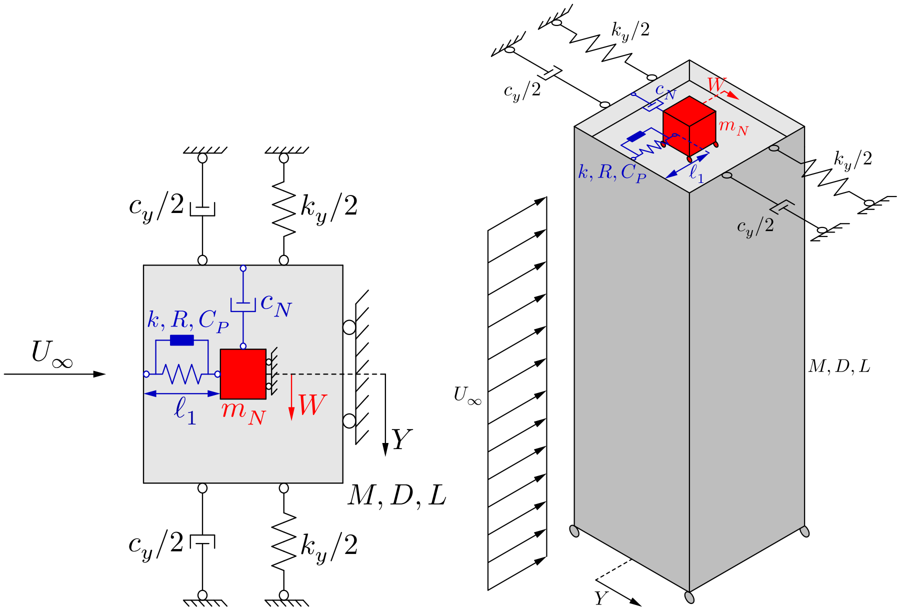

(a) 3D sketch (b) 3D sketch

In addition to the expressions shown in Eqs. 3–5, the virtual work of the non-conservative terms is needed for deriving the mathematical model. This quantity is given by Eq. 6.

$$\begin{aligned}\delta W_{nc} &= (F_y - c_y Y')\delta Y + (-c_N W')\delta W + Q\delta V \\ &= \hat{Q}_1 \delta Y + \hat{Q}_2 \delta W + \hat{Q}_3 \delta V \qquad (6)\end{aligned}$$

where F_y is the aerodynamic force associated with the galloping phenomenon and $\hat{Q}_i$ $(i = 1, 2, 3)$ represents the generalized force associated with the coordinates Y, W and V.

Using the classical quasi-steady approach (see, for example, [1]), the aerodynamic force coefficient C_y can be obtained either from experiments or from numerical simulations with a fixed body under different angles of attack. With these values, a polynomial function can be employed for fitting the data. The coefficients of this polynomial function A_n depend on the geometry on the cross-section and properties of the incoming flow, among other aspects.

For the oscillating prism under galloping, the instantaneous angle of attack is proportional to Y'/U_∞. In this paper, a seventh-order polynomial function is adopted and, hence, the aerodynamic force is given by Eq. 7.

$$\begin{aligned}F_y &= \frac{1}{2}\rho U_\infty^2 DLC_y \\ &= \frac{1}{2}\rho U_\infty^2 DL \sum_{n=1}^{7} A_n \left(\frac{Y'}{U_\infty}\right)^n \qquad (7)\end{aligned}$$

Following [41], the Euler-Lagrange equations for the solid–fluid-electric system is given by:

$$\frac{d}{dt}\left(\frac{\partial \mathcal{T}}{\partial q_i'}\right) - \frac{\partial \mathcal{T}}{\partial q_i} + \frac{\partial \mathcal{U}}{\partial q_i} - \frac{\partial \mathcal{W}}{\partial q_i} = \hat{Q}_i \qquad (8)$$

where $i = 1, 2, 3$ and $\boldsymbol{q} = \{q_1\ q_2\ q_3\}^T = \{Y\ W\ V\}^T$ is the vector that gathers the generalized coordinates. After some algebraic work, Eqs. 9–11 are obtained as the governing equations of the solid–fluid-electric system.

$$\begin{aligned}&(M + m_N)Y'' + m_N W'' + c_y Y' + k_y Y \\ &\quad = \frac{1}{2}\rho U_\infty^2 DLC_y \qquad (9)\end{aligned}$$

$$\begin{aligned}&m_N(Y'' + W'') + c_N W' \\ &\quad + kW\left(1 - \frac{\ell_0}{\sqrt{\ell_1^2 + W^2}}\right) - 2\theta V \frac{W}{\sqrt{\ell_1^2 + W^2}} = 0 \qquad (10)\end{aligned}$$

$$-2\theta\left(\sqrt{\ell_1^2 + W^2} - \ell_0\right) - C_P V = Q \qquad (11)$$

Taking the derivative of Eq. 11 with respect to time and recalling the constitutive equation $Q' = V/R$, one obtains:

$$C_P V' + \frac{V}{R} + 2\theta W' \left(\frac{W}{\sqrt{\ell_1^2 + W^2}} \right) = 0 \tag{12}$$

For the sake of generality, the equations of motion are rewritten in the dimensionless form. For this, we define $V_0 = \frac{m_N \omega^2 \ell_1}{2\theta}$ and $\omega = \sqrt{\frac{k_y}{M+m_n}}$ as reference values of electric tension and frequency, respectively. In addition, the dimensionless displacements y and w and electric tension v are defined as $y = Y/D$, $w = W/\ell_1$ and $v = V/V_0$. By adopting the quantities shown in Eq. 13, the dimensionless mathematical model is given by Eqs. 14–16.

$$\begin{aligned} & m^* = \frac{m_N + M}{\rho D^2 L}, \hat{m} = \frac{m_N}{m_N + M}, \\ & U_r = \frac{U_\infty}{\omega D}, \alpha = \frac{\ell_0}{\ell_1}, \beta = \frac{D}{\ell_1}, \kappa = \frac{k}{m_N \omega^2} \\ & \zeta_N = \frac{c_N}{2 m_N \omega}, \zeta_y = \frac{c_y}{2(M + m_N)\omega}, \\ & \sigma_1 = \frac{4\theta^2}{C_P m_N \omega^2}, \sigma_2 = \frac{1}{R C_P \omega} \end{aligned} \tag{13}$$

$$\begin{aligned} & \ddot{y} + \frac{\hat{m}}{\beta} \ddot{w} + 2\zeta_y \dot{y} + y \\ & \quad = \frac{1}{2} \frac{U_r^2}{m^*} \left(\sum_{n=1}^{7} A_n \left(\frac{\dot{y}}{U_r} \right)^n \right) \end{aligned} \tag{14}$$

$$\begin{aligned} & \beta \ddot{y} + \ddot{w} + 2\zeta_N \dot{w} \\ & \quad + \kappa \left(1 - \frac{\alpha}{\sqrt{1 + w^2}} \right) w - \frac{v w}{\sqrt{1 + w^2}} = 0 \end{aligned} \tag{15}$$

$$\dot{v} + \sigma_1 \frac{w \dot{w}}{\sqrt{1 + w^2}} + \sigma_2 v = 0 \tag{16}$$

where $\dot{(\,)}$ indicates the derivative with respect to the dimensionless time $\tau = \omega t$.

3 Analysis methodology

The dimensionless mathematical model governed by Eqs. 14–16 is numerically integrated in the interval $0 \leq \tau \leq 5000$ using the package DifferentialEquations.jl [58], developed for Julia Language Programming. In this package, the user can both specify the solver or let the algorithm choose the proper one. The second option is employed herein.

The simulations cover the interval of reduced velocities $8 \leq U_r \leq 50$ with 150 evenly spaced values. Notice that the validity of the quasi-steady hypothesis implies that the vortex-shedding frequency is much larger than the natural frequency of oscillation (see, for example, [1]). According to the latter reference, this hypothesis holds if $U_r > 20/(2\pi) = 3.18$.

Aiming at inducing bistability, the piezoelectric spring must be pre-compressed when $w = 0$. This is achieved by taking $\alpha = \ell_0/\ell_1 > 1$. The latter condition leads to three equilibrium positions for the device, namely, $w_0 = 0$, $w_0 = \sqrt{\alpha^2 - 1}$ and $w_0 = -\sqrt{\alpha^2 - 1}$. Appendix A brings some discussions regarding bistability in a simpler, albeit representative problem.

For all simulations, the only non-trivial initial conditions are $y(0) = 0.1$ and $w(0) = w_0 = \sqrt{\alpha^2 - 1}$ if $\alpha > 1$ or $w(0) = w_0 = 0$ if $\alpha \leq 1$. Note that initial conditions may play an important role in the dynamics of nonlinear systems. However, since the dimension of the phase space is 5, computing these basins of attraction is not a trivial task, but can be explored in further works.

Notice that, as the initial conditions are the same in all the simulations, the hysteresis phenomenon that can be potentially observed when the reduced velocity is increased or decreased cannot be captured. Such aspect would be observed in a classical bifurcation diagram, in which the initial conditions for the i^{th} value of the bifurcation parameter depend on the response of the obtained for the $(i-1)^{\text{th}}$ value of the mentioned parameter.

Due to the large number of parameters of the mathematical model, a reference configuration is defined. The following structural parameters of the prism are extracted from the wind tunnel experimental investigation on the passive suppression of galloping described in [21,22]: $M = 1.39$ kg, $L = 58$ cm, $D = 5$ cm, $k_y = 360$ N/m, $\zeta_y = 0.01$. From the same references, $\hat{m} = 0.08$ is considered as the dimensionless mass of the suppressor. We also assume $\rho = 1.225$ kg/m^3, leading to $m^* = 850.6$. The parameters of the energy harvesting circuit are the same as presented in [44], namely $\theta = 1.55 \times 10^{-3}$ N/V, $C_P = 120 \times 10^{-9}$ F and $R = 10^4$ Ω. The use of these values of θ, C_P and R yields $\sigma_1 = 2.78$ and $\sigma_2 = 53.99$. The remainder parameters which characterize the device, namely its damping constant, stiffness and nonlinearity level (ζ_N, κ and α, respectively) are defined after the analysis of stability of the equilibrium condition, discussed in greater depth in Sect. 4.1.

The values of the aerodynamic coefficients A_n are obtained from the experimental data with a static prism presented in [23]. In the latter reference, a statistical analysis was performed to remove a systematic error intrinsic in the measurements of the aerodynamic force. Figure 2 shows the experimental data extracted from [23] (properly reflected with respect to 0). From these values, the coefficients of the polynomial fit are obtained as $A_1 = 2.9828$, $A_3 = -32.7051$, $A_5 = -52.1758$, $A_7 = 409.3566$ and $A_2 = A_4 = A_6 = 0$.

Now, the methodologies for the signal analyses are discussed. Prism oscillation amplitude $\hat{y}$ is calculated using Eq. 17.

$$\hat{y} = \sqrt{2} y_{std} \tag{17}$$

where y_{std} is the standard deviation of $y(\tau)$ evaluated while considering only $\tau \geq 2500$. This avoids including the initial transient in the statistic calculated. For the same reason, the standard deviation of $v(\tau)$ (v_{std}) and all the calculated amplitude spectra, obtained with the Fast Fourier Transform algorithm implemented into the FFTW Julia package, also disregard the mentioned initial transitory. In the amplitude spectra, $\hat{\omega}$ is the oscillation frequency normalized with respect to the reference frequency ω. Note that if the prism response $y(\tau)$ is harmonic and monochromatic, Eq. 17 leads to the exact value of oscillation amplitude.

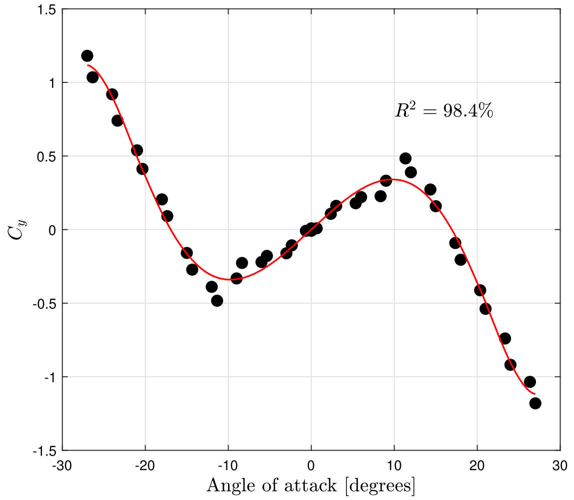

Fig. 2 Cross-wise force coefficient as a function of the angle of attack for the static prism. Experimental data from [23] and 7th-order polynomial fit

In order to facilitate the assessment of the suppression efficiency, the same criterion adopted in [15] is considered. In this criterion, parameter $\hat{S}$ is defined as:

$$\hat{S} = 1 - \frac{\hat{y}}{\hat{y}_0} \tag{18}$$

where $\hat{y}$ is the characteristic oscillation amplitude of the prism fitted with the device (calculated using Eq. 17) and $\hat{y}_0$ is the characteristic oscillation amplitude of the prism for the case in which the prism is not fitted with the suppressor/energy harvester device. The latter case in herein indicated as Pure Galloping.

4 Results and discussion

This section is divided into three subsections. Subsection 4.1 presents a study on the stability of the equilibrium solution, which is important for defining the values of κ, α and ζ_N to be considered in the numerical simulations. Section 4.2 discusses the influence of the nonlinearity parameter α. Finally, analytical considerations based on a perturbation method are made in Sect. 4.3.

4.1 Stability analysis

We firstly investigate the influence of some of the suppressor parameters on the critical reduced velocity associated with the galloping phenomenon U_r^c. For this, we define $\boldsymbol{x} = \{x_1\ x_2\ x_3\ x_4\ x_5\}^T = \{y\ w\ v\ \dot{y}\ \dot{w}\}^T$. Using this nomenclature, the equilibrium of Eqs. 14–16 corresponds to $\boldsymbol{x_0} = \{x_{1,0}\ x_{2,0}\ x_{3,0}\ x_{4,0}\ x_{5,0}\}^T = \{0\ w_0\ 0\ 0\ 0\}^T$, where $w_0 = \pm\sqrt{\alpha^2 - 1}$ or $w_0 = 0$ if $\alpha > 1$ and $w_0 = 0$ if $\alpha \leq 1$. Note that w_0 is an unstable equilibrium point for $\alpha > 1$.

We define disturbances around the equilibrium points as $\delta x_i = x_i - x_{i,0}$ ($i = 1, \ldots, 5$) and $\boldsymbol{\delta \dot{x}} = \{\delta x_1\ \ \delta x_2\ \ \delta x_3\ \ \delta x_4\ \ \delta x_5\}^T$. Considering small disturbances, the temporal evolution of δx_i are governed by Eq. 19.

$$\boldsymbol{\delta \dot{x}} = \boldsymbol{\mathcal{J} \delta x} \tag{19}$$

where

$$
\mathcal{J}=\begin{pmatrix}
0 & 0 & 0 & 1 & 0\\
0 & 0 & 0 & 0 & 1\\
0 & 0 & -\sigma_2 & 0 & \frac{\sigma_1 x_{2,0}}{\sqrt{x_{2,0}^2+1}}\\
-\frac{1}{1-\hat{m}} & -\frac{\hat{m}\gamma}{\beta(1-\hat{m})} & -\frac{\hat{m}x_{2,0}}{\beta(1-\hat{m})\sqrt{x_{2,0}^2+1}} & \frac{\frac{A_1U_r}{2m^*}-2\zeta_y}{1-\hat{m}} & \frac{2\hat{m}\zeta_N}{\beta(1-\hat{m})}\\
\frac{\beta}{1-\hat{m}} & \frac{\gamma}{1-\hat{m}} & \frac{x_{2,0}}{(1-\hat{m})\sqrt{x_{2,0}^2+1}} & -\frac{\beta\left(\frac{A_1U_r}{2m^*}-2\zeta_y\right)}{1-\hat{m}} & -\frac{2\zeta_N}{1-\hat{m}}
\end{pmatrix} \tag{20}
$$

is the Jacobian matrix of the system given by Eqs. 14–16 and auxiliary quantity γ reads:

$$
\gamma=-\frac{\alpha\kappa x_{2,0}^2}{\left(x_{2,0}^2+1\right)^{3/2}}-\kappa\left(1-\frac{\alpha}{\sqrt{x_{2,0}^2+1}}\right) \tag{21}
$$

The classical Lyapunov's indirect method is employed for investigating the stability of the equilibrium condition. For this, let λ_i $(i=1,\ldots,5)$ be the eigenvalues of $\mathcal{J}$. Notice that $\mathcal{J}$ depends on several parameters, including device mass $\hat{m}$, damping ζ_N, stiffness κ, aerodynamic coefficient A_1 and reduced velocity U_r. Here, $\beta=0.5$ and $\hat{m}=0.08$ are kept fixed and the critical reduced velocity U_r^c is calculated for different values of α, ζ_N and κ by inspecting the lowest value of U_r that produces $\mathrm{Re}\{\lambda_i\}>0$.

Figure 3 shows the results from the stability analysis. In this figure, the domain $1\leq\kappa\leq 15\times 0.5\leq\alpha\leq 1.5\times 0.05\leq\zeta_N\leq 0.15$ is discretized using a $300\times 200\times 50$ grid. In Fig. 3a, the colorbar represents the ratio between U_r^c and the critical reduced velocity for the Pure Galloping case $U_0=4\zeta_y m^*/A_1=11.41$. Figure 3b–d illustrates cross-sections of the 3D map obtained by considering $\zeta_N=0.072$, $\zeta_N=0.099$ and $\zeta_N=0.124$, respectively.

As indicated in Fig. 3, there is a narrow region of the space of control parameters (κ,α,ζ_N) in which a marked increase in the critical reduced velocity for the Hopf bifurcation is seen. For passive suppression appli-

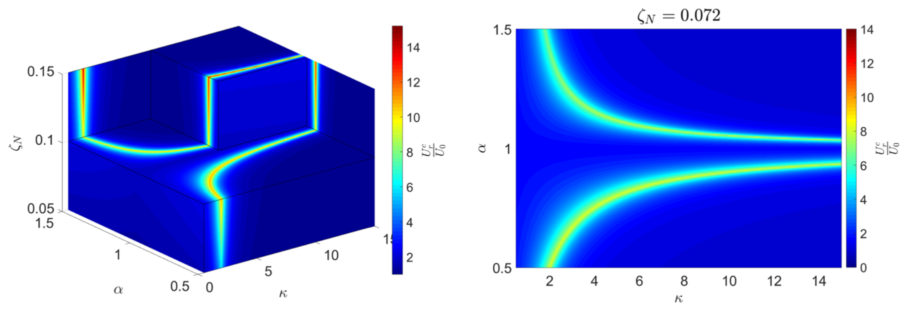

(a) $U_r^c(\kappa,\alpha,\zeta_N)/U_0$.

(b) $U_r^c(\kappa,\alpha,\zeta_N=0.072)/U_0$.

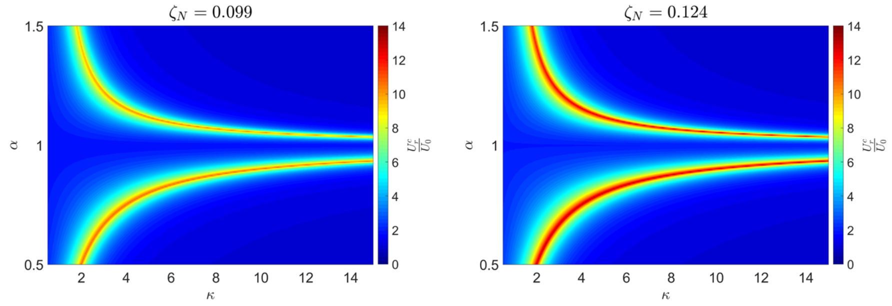

(c) $U_r^c(\kappa,\alpha,\zeta_N=0.099)/U_0$.

(d) $U_r^c(\kappa,\alpha,\zeta_N=0.124)/U_0$.

Fig. 3 Results from the stability analysis

Table 1 Dimensionless parameters of the device investigated

Parameter	Value	Parameter	Value	Parameter	Value
$\hat{m}$	0.08	m^*	850.6	ζ_y	0.01
ζ_N	0.10	σ_1	2.78	σ_2	53.99
α	1.5 and 0.5	β	0.5	κ	9

cations, the choice of the control parameters in this mentioned narrow region is of interest, since it corresponds to a marked increase in the critical reduced velocity. In turn, for energy harvesting applications, postponing the galloping phenomenon is undesired, since the source of energy to be converted into electricity is the oscillatory response of the prism.

Aiming at balancing passive suppression of galloping and energy harvesting, the values of α, κ and ζ_N are chosen such that no significant increase in the critical reduced velocity is observed. Using this criterion and based on the stability maps presented in Fig. 3, we define $\zeta_N = 0.1$ and $\kappa = 9$. Two values of α are investigated for assessing the role of the bistability on the device performance, namely $\alpha = 1.5$ ($U_r^c/U_0 = 1.04$) and $\alpha = 0.5$, which leads to $U_r^c/U_0 = 1.06$.

Table 1 summarizes the dimensionless values of the parameters that define the suppressor/energy harvester device.

4.2 Influence of nonlinearity parameter α

Figure 4 shows the variation of both characteristic oscillation amplitude of the prism $\hat{y}$ and suppression efficiency $\hat{S}$ with reduced velocity U_r. The oscillation amplitudes obtained with $\alpha = 0.5$ (monostable system) are slightly smaller than those from the Pure Galloping case. Quantitatively, the suppression efficiency is $\hat{S} < 0.2$ for $U_r \geq 15$. In turn, the BSPNES with $\alpha = 1.5$ allows for significant suppression in the interval $15 \leq U_r \leq 35$, where $\hat{y} \approx 2$. Still considering $\alpha = 1.5$, a sudden loss of suppression efficiency is observed around $U_r = 35$ and, after this value of reduced velocity, curve $\hat{y}(U_r)$ follows that from Pure Galloping, but with some reduction in the characteristic oscillation amplitude.

To complement the discussions regarding the prism response, examples of time histories $y(\tau)$ and $w(\tau)$ and the corresponding amplitude spectra are analyzed as from Figs. 5 and 6. In these figures, two values of reduced velocity are considered, namely $U_r = 27.45$ and $U_r = 42.95$. Notice that these values are lower and higher than $U_r = 35$, associated with the jump in the $\hat{y}(U_r)$ plot for the BSPNES (see Fig. 4a).

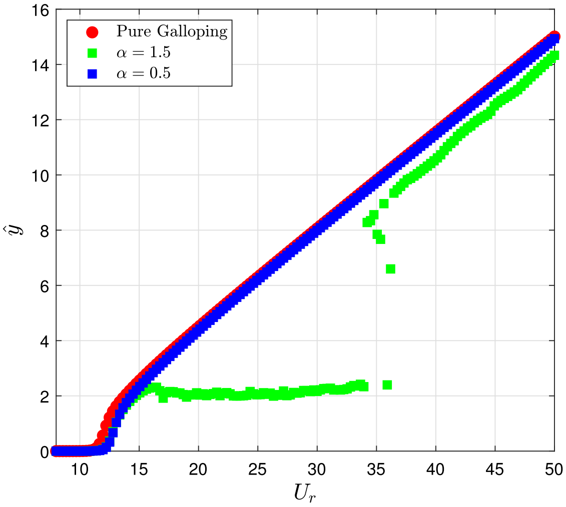

(a) $\hat{y}$

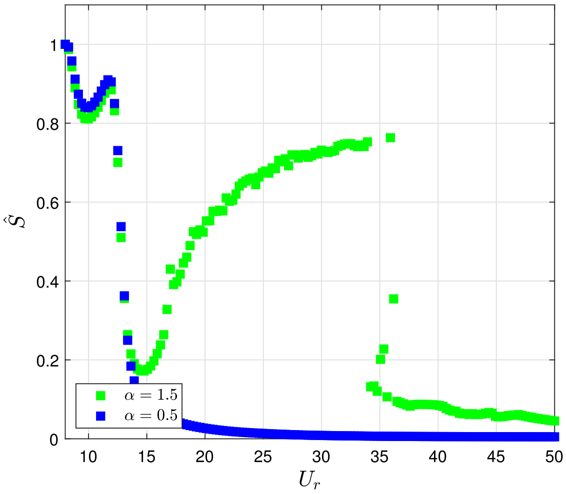

(b) $\hat{S}$

Fig. 4 Suppression efficiency $\hat{y}$ as a function of reduced velocity U_r for different values of nonlinearity parameter α. $\hat{m} = 0.08$, $m^* = 850.6$, $\zeta_y = 0.01$, $\zeta_N = 0.10$, $\kappa = 9$, $\sigma_1 = 2.78$, $\sigma_2 = 53.99$ and $\beta = 0.5$

For $U_r = 27.45$, Fig. 5a shows a strongly modulated response for the prism, a behavior previously observed in passive suppression of vibrations using NESs. Amplitude spectrum $A(\hat{\omega})$ shown in Fig. 5a exhibits energy distribution for different frequencies, even though a dominant one $\hat{\omega} \approx 1$ clearly appears.

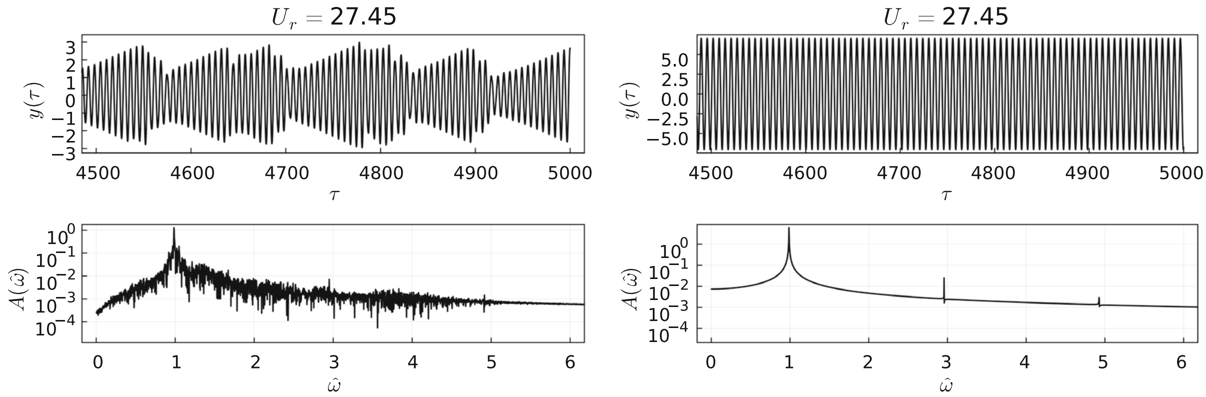

(a) $\alpha = 1.5,\ U_r = 27.45$.

(b) $\alpha = 0.5,\ U_r = 27.45$.

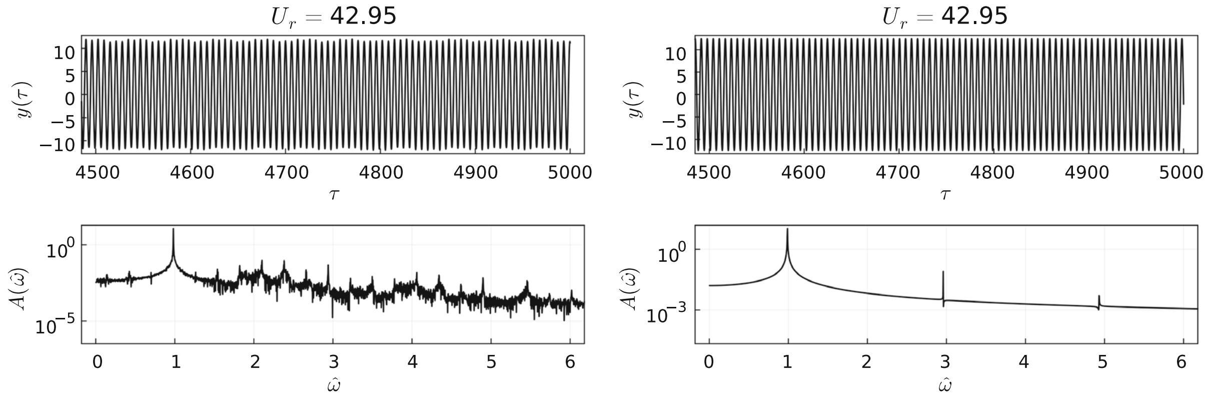

(c) $\alpha = 1.5,\ U_r = 42.95$.

(d) $\alpha = 0.5,\ U_r = 42.95$.

Fig. 5 Examples of time histories $y(\tau)$. For the sake of visualization, the scales are not the same in all plots. Only the time window $4500 \leq \tau \leq 5000$ is shown

Now considering the monostable system with $\alpha = 0.5$, Fig. 5b reveals the existence of steady-state oscillations, defined by a narrowbanded amplitude spectrum of dominant frequency $\hat{\omega} \approx 1$. For reduced velocity $U_r = 42.95$, Fig. 5c and d indicate responses $y(\tau)$ practically free from amplitude modulation and with similar characteristic values $\hat{y}$ and dominant frequency $\hat{\omega} \approx 1$. Despite these similarities mentioned, the amplitude spectra have distinct qualitative behaviors, the one from the BSPNES with $\alpha = 1.5$ showing a richer spectral content.

Device response $w(\tau)$ obtained from the BSPNES with $\alpha = 1.5$ at reduced velocity $U_r = 27.45$ is shown in Fig. 6a. The joint analysis of Figs. 5a and 6a reveals that the strongly modulated responses of the prism are associated with oscillations around the equilibrium points $w_0 = \pm 1.12$ during the phase in which $y(\tau)$ increases. When these oscillations reach a certain value, the device is captured for oscillating around the other equilibrium point in a process that accounts for decreasing the prism response. Such behavior is quite different from the one observed for the monostable system, characterized by the steady-state oscillations of the device.

For $U_r = 42.95$, BSPNES response $w(\tau)$ shown in Fig. 6c covers the two equilibrium points (interwell oscillations), with some amplitude modulation that justifies the several peaks that appear in the amplitude spectra calculated from the prism response depicted in Fig. 5c. Note that even though the interwell oscillations shown in Fig. 6c exhibit larger amplitudes, the transient responses associated with switches at the equilibrium

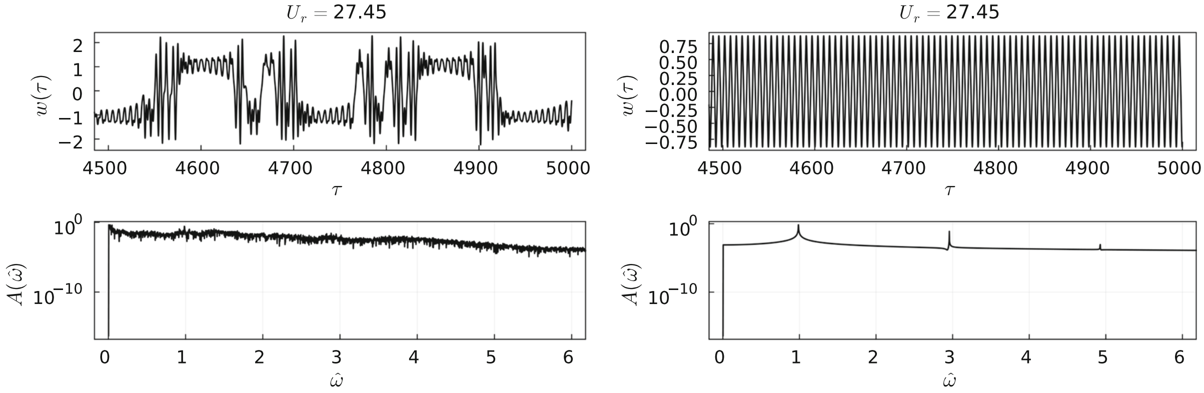

(a) $\alpha = 1.5$, $U_r = 27.45$. (b) $\alpha = 0.5$, $U_r = 27.45$.

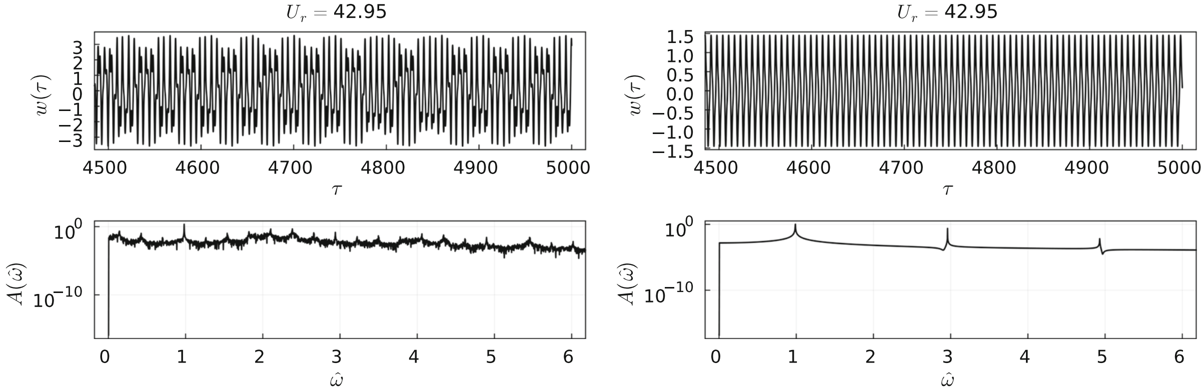

(c) $\alpha = 1.5$, $U_r = 42.95$. (d) $\alpha = 0.5$, $U_r = 42.95$.

Fig. 6 Examples of time histories $w(\tau)$. For the sake of visualization, the scales are not the same in all plots. Only the time window $4500 \leq \tau \leq 5000$ is shown

points around which the device oscillates define more favorable scenarios for passive suppression.

The variation of the root-mean square electric tension with the reduced velocity is illustrated in Fig. 7. The values of v_{std} obtained from the monostable system with $\alpha = 0.5$ monotonically increase from 0 for $U_r \leq U_r^c$ to $v_{std} = 0.04$ at $U_r = 50$. For the BSPNES, the values of v_{std} also monotonically increase from 0 to $v_{std} \approx 0.04$ when the reduced velocity varies in the interval $U_r^c \leq U_r \leq 35$. Notice that, in the latter interval, the energy harvesting efficiency (if measured by v_{std}) is much larger for the BSPNES, despite the smaller responses of the prism. Hence, it can be concluded that bistability can be employed in the design of a device that has superior performance in terms of both passive suppression of oscillations and energy harvesting. Energy harvesting and passive suppression may seem to be competing aspects, since the decrease in the structural response decreases the amount of energy to be harvested. However, in the solution herein investigated, the source of energy is the device motion instead of the response of the main structure.

Examples of time histories $v(\tau)$ are illustrated in Fig. 8. For the monostable system, Fig. 8b and d indicate the existence of steady-state oscillations, in agreement with corresponding time histories $w(\tau)$ shown in Fig. 6b and d. In contrast to what is observed for device response $w(\tau)$, dimensionless electric tension $v(\tau)$ has dominant frequency $\hat{\omega} \approx 2$ (twice the dominant frequency of $w(\tau)$). As expected, the qualitative aspect of time histories $v(\tau)$ obtained from the BSPNES (see Fig. 8a and c) also agrees with that from the

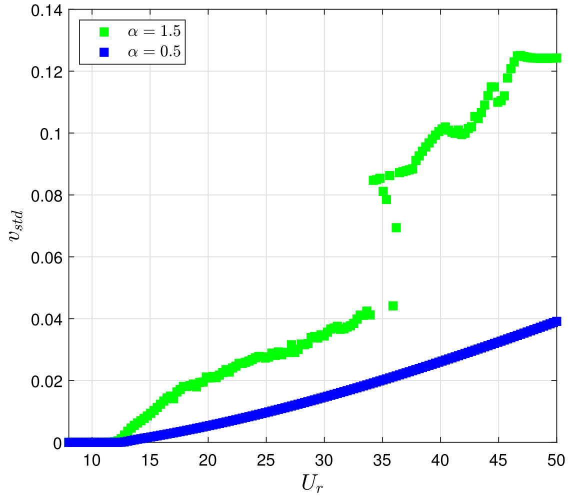

Fig. 7 Standard deviation of the harvested electric tension as a function of reduced velocity U_r for different values of nonlinearity parameter α. $\hat{m} = 0.08$, $\hat{m}^* = 850.6$, $\zeta_y = 0.01$, $\zeta_N = 0.10$, $\kappa = 9$, $\sigma_1 = 2.78$, $\sigma_2 = 53.99$ and $\beta = 0.5$

associated device response $w(\tau)$ shown in Fig. 6a and c.

This section is concluded with the analysis of selected trajectories in the phase space. Since the phase space has dimension 5, such analyses consider points in the Poincaré section Σ defined by Eq. 22. Notice that the defined Poincaré section allows obtaining both positive and negative values of $y(\tau)$ (two-sided Poincaré section).

$$\Sigma = \{(y, w, v, \dot{y}, \dot{w}) \in \mathbb{R}^5 : \dot{y} = 0\} \tag{22}$$

Figure 9 presents projections of the trajectories onto the $w(\tau) \times \dot{w}(\tau)$ plane and the corresponding points on the Poincaré section, represented by the green circles. In this plot, the initial transitory is not shown. As indicated in Figs. 9a and c, the trajectories obtained with the BSPNES densely fill the corresponding region of the $w(\tau) \times \dot{w}(\tau)$ plane, with a cloud of points in the Poincaré section. In turn, Fig. 9b and d reveal well-defined closed curve for the monostable system with $\alpha = 0.5$.

A more complete description of the dynamics of the solid–fluid-electric system is depicted in Fig. 10, which illustrates projections of the trajectories onto the space $y(\tau) \times w(\tau) \times \dot{w}(\tau)$, the points on the Poincaré section and the values of $v(\tau)$. Indeed, the illustrated responses from the monostable system are periodic (see Fig. 10b and d), while those from the BSPNES do not exhibit any regular pattern and densely fill a set of the phase space.

4.3 Asymptotic analysis

A perturbation procedure is applied to Eqs. 14–16. The dynamical system under analysis presents a strong nonlinear feature in Eq. 15, related to parameter α: more specifically, as $\alpha \rightarrow 1$, the linear stiffness of the absorber goes to zero, actually becoming an essentially nonlinear oscillator. A possible way to deal with this occurrence with perturbation methods is using the Multiple Scale-Harmonic Balance Method (MSHBM), introduced in [59] for externally forced main systems embedded with a NES, and then extended to aerodynamic systems in [25]. Then, a combination of Multiple Scale Method (MSM) and Harmonic Balance (HB) is made, where the HB is only used for the NES equation, whereas the well-known features of system filtering and reduction to the normal form of bifurcation are left to the MSM for the main system. Other possibilities include using the Complexification Averaging (CX-A), as in [32].

The case under study in this paper requires an improvement of the cited method, associated with the bistable nature of the system. For the specific case, the perturbation analysis is performed for either oscillations of the absorber around the trivial equilibrium configuration at $\alpha \leq 1$ or intrawell oscillations, around one of the non-trivial equilibrium configurations for $\alpha > 1$, leaving the much more complicated perturbation analysis of interwell oscillations [60], which are detected for instance in Fig. 6a, to future developments. More specifically, for the two cases analyzed, i.e. far from $\alpha = 1$, the absorber has a linearizable nature although the MSHBM appears as a reliable tool as well. The improvement of the method herein proposed derives from the multiple scale analysis performed for a weakly nonlinear thermo-mechanical system in [61], where oscillations around non-trivial equilibrium configurations are sought.

To perform the perturbation analysis, parameters are rescaled, after introducing a small book-keeping parameter $\epsilon > 0$:

$$\begin{aligned} &\hat{m} \rightarrow \epsilon \hat{m}, \quad \sigma_1 \rightarrow \epsilon \sigma_1, \\ &A_3 \rightarrow \frac{A_3}{\epsilon}, \quad A_5 \rightarrow \frac{A_5}{\epsilon^3}, \quad A_7 \rightarrow \frac{A_7}{\epsilon^5}, \end{aligned} \tag{23}$$

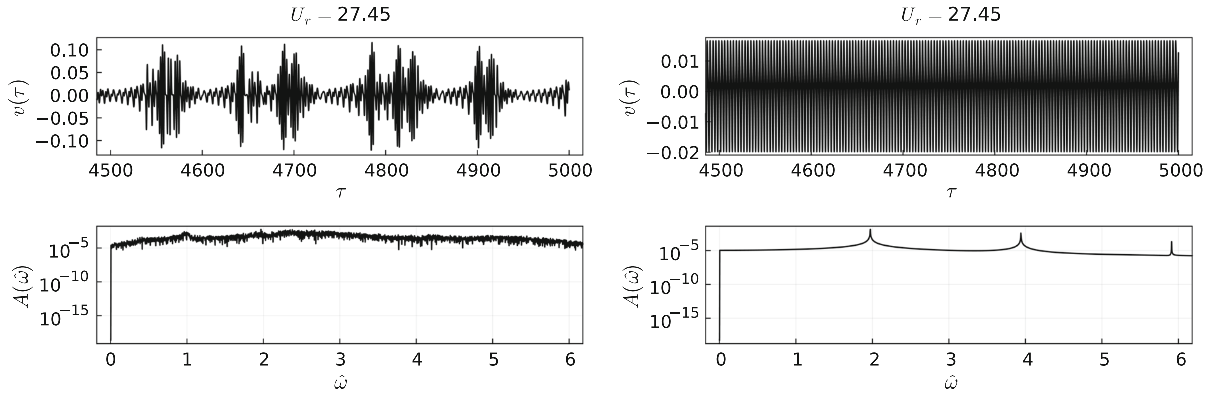

(a) $\alpha = 1.5$, $U_r = 27.45$. (b) $\alpha = 0.5$, $U_r = 27.45$.

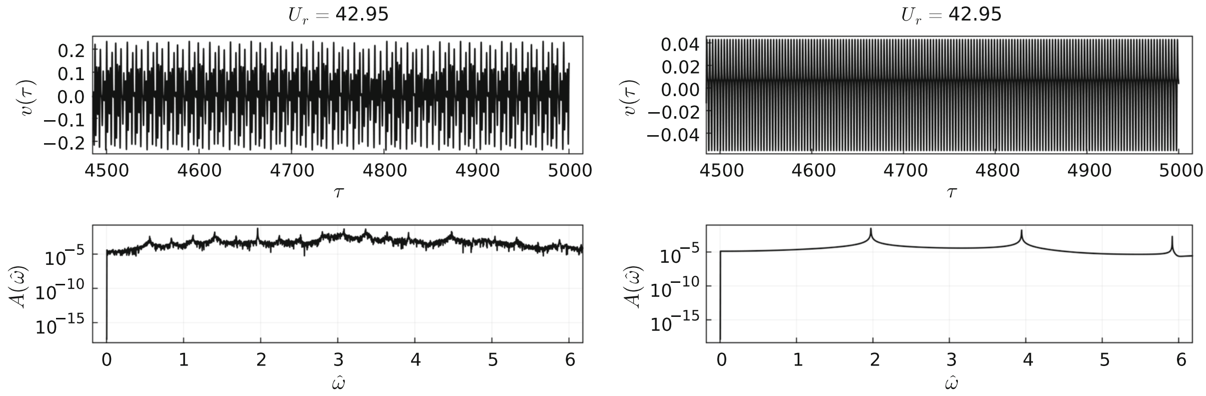

(c) $\alpha = 1.5$, $U_r = 42.95$. (d) $\alpha = 0.5$, $U_r = 42.95$.

Fig. 8 Examples of time histories $v(\tau)$. For the sake of visualization, the scales are not the same in all plots. Only the time window $4500 \leq \tau \leq 5000$ is shown

which is based on the actual order of magnitude of the parameters themselves and, moreover, lets the aerodynamic nonlinear terms concurrently appear at the same perturbation step in the prism equations, i.e. at order 2. A sliding term $\hat{U}$ is introduced as well for the reduced velocity, which represents the bifurcation parameter, namely:

$$U_r = U_0 + \epsilon \hat{U} \tag{24}$$

entailing that the response is analyzed in a neighborhood of velocity U_0. Note that U_0 corresponds to the (nondimensional) critical velocity of the prism with disconnected controlling device (Pure Galloping case).

Since oscillations around the trivial and nontrivial equilibrium configurations are sought, a sliding variable $\tilde{w}(\tau)$ is also introduced for $w(\tau)$, as follows:

$$w(\tau) = w_0 + \tilde{w}(\tau) \tag{25}$$

where w_0 is one of the equilibrium configurations defined in Sect. 4.1.

As even and odd nonlinear terms appear in the equations of motion, the following power expansion of the variables is introduced:

$$\begin{aligned} y &= \epsilon^1 y_1 + \epsilon^2 y_2 + \epsilon^3 y_3, \\ \tilde{w} &= \epsilon^1 w_1 + \epsilon^2 w_2 + \epsilon^3 w_3, \\ v &= \epsilon^2 v_2 + \epsilon^3 v_3, \end{aligned} \tag{26}$$

where variable v misses the term at order ϵ as it is assumed to contribute later to the perturbation scheme.

Three time scales are introduced:

$$t_0 = \tau, \quad t_1 = \epsilon \tau, \quad t_2 = \epsilon^2 \tau, \tag{27}$$

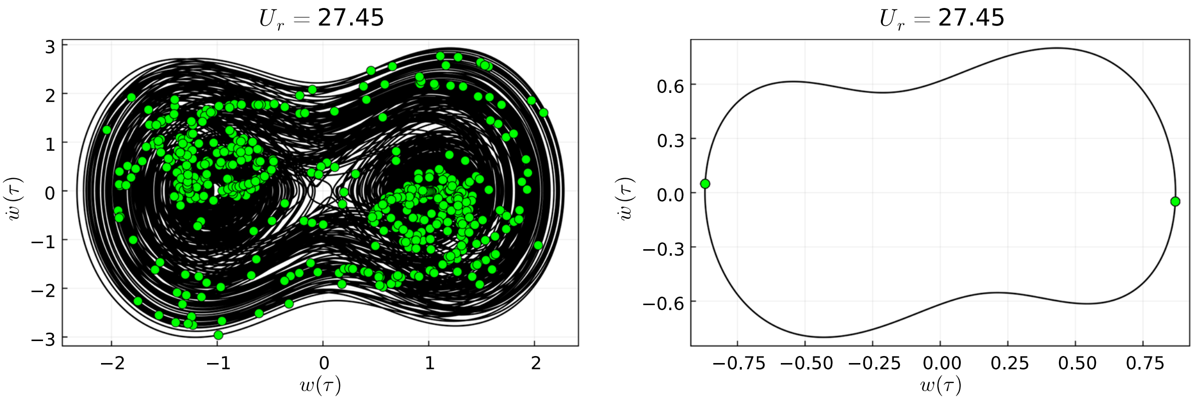

(a) $\alpha = 1.5$, $U_r = 27.45$. (b) $\alpha = 0.5$, $U_r = 27.45$.

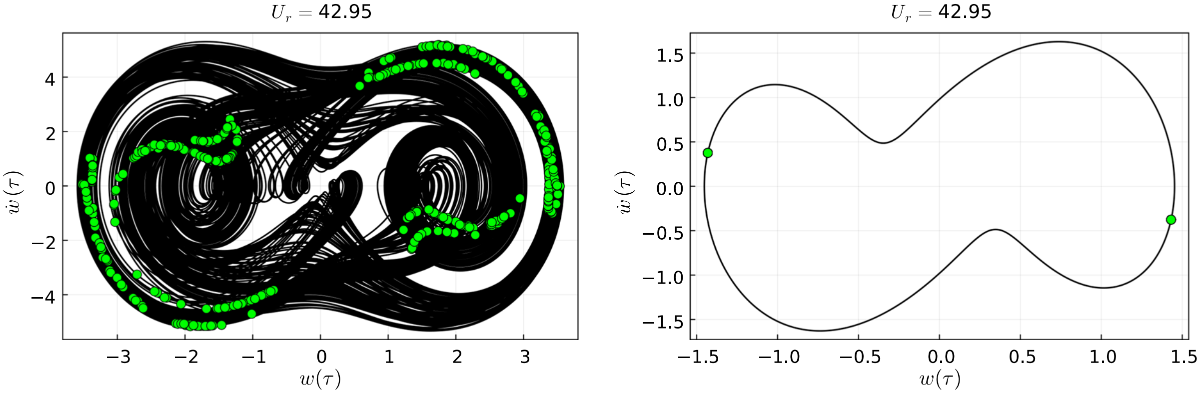

(c) $\alpha = 1.5$, $U_r = 42.95$. (d) $\alpha = 0.5$, $U_r = 42.95$.

Fig. 9 Projections of the trajectories onto the plane $w(\tau) \times \dot{w}(\tau)$. For the sake of visualization, the scales are not the same in all plots. The green circles correspond to points in the defined Poincaré section

and, consistently, three differential operators are defined as $d_j = \frac{d}{dt_j}$, $j = 0, 1, 2$, where:

$$\begin{aligned} \frac{d}{d\tau} &= d_0 + \epsilon d_1 + \epsilon^2 d_2, \\ \frac{d^2}{d\tau^2} &= d_0^2 + 2\epsilon d_0 d_1 + \epsilon^2 (d_1^2 + 2 d_0 d_2). \end{aligned} \tag{28}$$

Substituting Eqs. 23–28 into Eqs. 14–16, series expanding and collecting the terms with the same powers of ϵ, produce the following perturbation equations:
Order ϵ^0:

$$\kappa w_0 - \frac{\alpha \kappa w_0}{\sqrt{w_0^2 + 1}} = 0 \tag{29}$$

Order ϵ:

$$d_0^2 y_1 + y_1 = 0 \tag{30}$$

$$\beta d_0^2 y_1 + d_0^2 w_1 + 2\zeta_N d_0 w_1 + \kappa w_1 + \frac{\alpha \kappa w_0^2 w_1}{\left(w_0^2 + 1\right)^{3/2}} - \frac{\alpha \kappa w_1}{\sqrt{w_0^2 + 1}} = 0 \tag{31}$$

Order ϵ^2:

$$d_0^2 y_2 + y_2 = \frac{A_7 d_0 y_1^7}{2m^* U_0^5} + \frac{A_5 d_0 y_1^5}{2m^* U_0^3} + \frac{A_3 d_0 y_1^3}{2m^* U_0} + \frac{A_1 \hat{U} d_0 y_1}{2m^*}$$

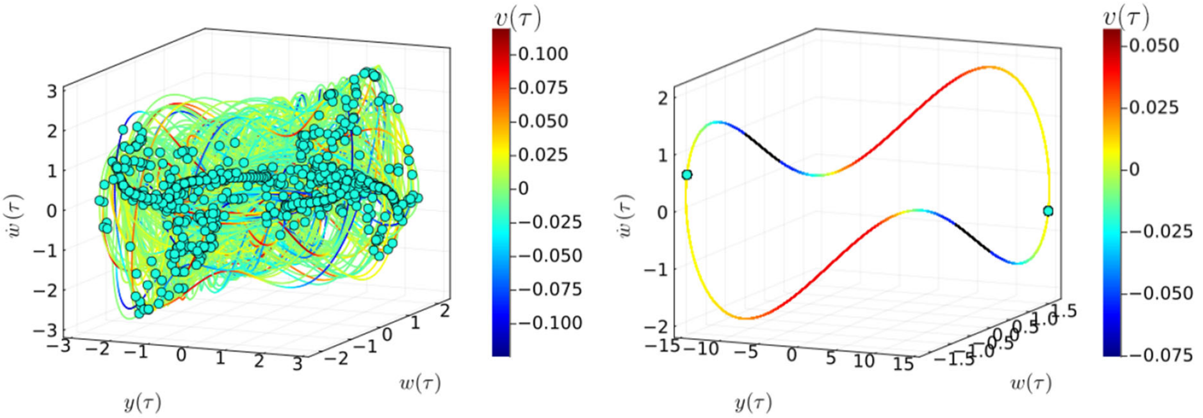

(a) $\alpha = 1.5$, $U_r = 27.45$. (b) $\alpha = 0.5$, $U_r = 27.45$.

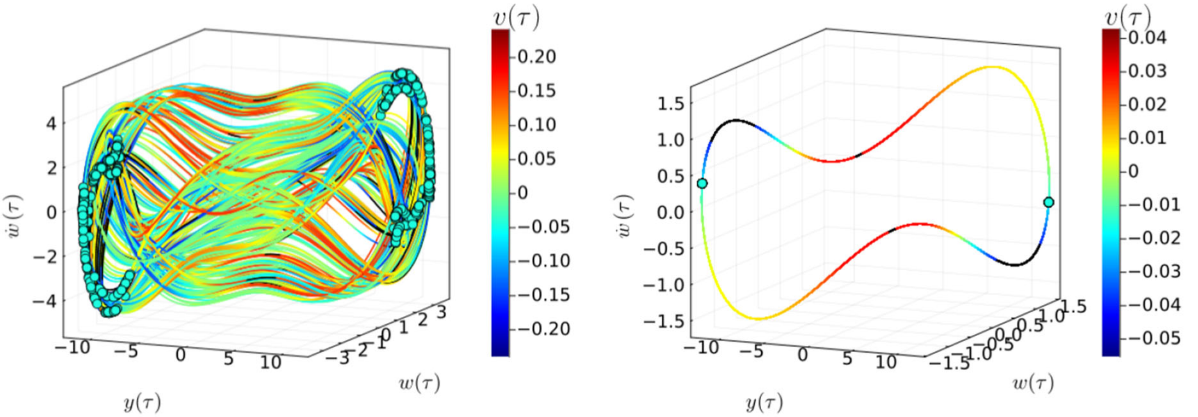

(c) $\alpha = 1.5$, $U_r = 42.95$. (d) $\alpha = 0.5$, $U_r = 42.95$.

Fig. 10 Projections of the trajectories onto the space $y(\tau) \times w(\tau) \times \dot{w}(\tau)$. For the sake of visualization, the scales are not the same in all plots. The green circles correspond to points in the defined Poincaré section and the colorbar indicates the values of $v(\tau)$

$$+ \frac{A_1 U_0 d_1 y_1}{2m^*} - \frac{\hat{m} d_0^2 w_1}{\beta} - 2\zeta_y d_1 y_1 - 2 d_0 d_1 y_1, \tag{32}$$

$$\beta d_0^2 y_2 + d_0^2 w_2 + 2\zeta_N d_0 w_2 + \kappa w_2 - \frac{\alpha\kappa w_2}{\sqrt{w_0^2+1}} = -2\beta d_0 d_1 y_1 - 2 d_0 d_1 w_1 - 2\zeta_N d_1 w_1 - \frac{\alpha\kappa w_0^4 w_2}{\left(w_0^2+1\right)^{5/2}} + \frac{\alpha\kappa w_0^3 w_1^2}{\left(w_0^2+1\right)^{5/2}} - \frac{\alpha\kappa w_0^2 w_2}{\left(w_0^2+1\right)^{5/2}} - \frac{\alpha\kappa w_0 w_1^2}{\left(w_0^2+1\right)^{3/2}} - \frac{\alpha\kappa w_0 w_1^2}{2\left(w_0^2+1\right)^{5/2}} + \frac{w_0 v_2}{\sqrt{w_0^2+1}}, \tag{33}$$

$$d_0 v_2 + \sigma_2 v_2 = -\frac{\sigma_1 w_0 d_0 w_1}{\sqrt{w_0^2+1}}, \tag{34}$$

Order ϵ^3:

$$d_0^2 y_3 + y_3 = -\frac{5\hat{U} A_7 d_0 y_1^7}{2m^* U_0^6} + \frac{7 d_0 y_2 A_7 d_0 y_1^6}{2m^* U_0^5} + \frac{7 d_1 y_1 A_7 d_0 y_1^6}{2m^* U_0^5} - \frac{3\hat{U} A_5 d_0 y_1^5}{2m^* U_0^4} + \frac{5 d_0 y_2 A_5 d_0 y_1^4}{2m^* U_0^3} + \frac{5 d_1 y_1 A_5 d_0 y_1^4}{2m^* U_0^3} - \frac{\hat{U} A_3 d_0 y_1^3}{2m^* U_0^2}$$

$$
\begin{aligned}
&+\frac{3d_0y_2A_3d_0y_1^2}{2m^*U_0}\\
&+\frac{3d_1y_1A_3d_0y_1^2}{2m^*U_0}-\frac{\hat{m}d_0^2w_2}{\beta}-2d_0d_1y_2\\
&-\frac{2\hat{m}d_0d_1w_1}{\beta}-d_1^2y_1\\
&-2d_0d_2y_1+\frac{\hat{U}d_0y_2A_1}{2m^*}+\frac{\hat{U}d_1y_1A_1}{2m^*}+\frac{d_1y_2A_1U_0}{2m^*}\\
&+\frac{d_2y_1A_1U_0}{2m^*}\\
&-2\zeta_yd_1y_2-2\zeta_yd_2y_1, \qquad (35)
\end{aligned}
$$

$$
\begin{aligned}
&\beta d_0^2y_3+d_0^2w_3+2\zeta_Nd_0w_3+\kappa w_3\\
&-\frac{\alpha\kappa w_3}{\sqrt{w_0^2+1}}+\frac{\alpha\kappa w_3w_0^2}{\left(w_0^2+1\right)^{3/2}}=\\
&-\frac{5\alpha\kappa w_1^3w_0^4}{2\left(w_0^2+1\right)^{7/2}}+\frac{2\alpha\kappa w_1w_2w_0^3}{\left(w_0^2+1\right)^{5/2}}\\
&+\frac{5\alpha\kappa w_1^3w_0^2}{2\left(w_0^2+1\right)^{5/2}}-\frac{w_1v_2w_0^2}{\left(w_0^2+1\right)^{3/2}}\\
&-\frac{2\alpha\kappa w_1w_2w_0}{\left(w_0^2+1\right)^{3/2}}-\frac{\alpha\kappa w_1w_2w_0}{\left(w_0^2+1\right)^{5/2}}\\
&+\frac{v_3w_0}{\sqrt{w_0^2+1}}-\frac{\alpha\kappa w_1^3}{2\left(w_0^2+1\right)^{5/2}}\\
&-2\zeta_Nd_1w_2-2\beta d_0d_1y_2-2d_0d_1w_2\\
&-\beta d_1^2y_1-d_1^2w_1-2\zeta_Nd_2w_1\\
&-2\beta d_0d_2y_1-2d_0d_2w_1+\frac{w_1v_2}{\sqrt{w_0^2+1}}, \qquad (36)
\end{aligned}
$$

$$
\begin{aligned}
d_0v_3+v_3={}&\frac{d_0w_1\sigma_1w_1w_0^2}{\left(w_0^2+1\right)^{3/2}}\\
&-\frac{d_0w_2\sigma_1w_0}{\sqrt{w_0^2+1}}-\frac{d_1w_1\sigma_1w_0}{\sqrt{w_0^2+1}}-d_1v_2-\frac{d_0w_1\sigma_1w_1}{\sqrt{w_0^2+1}}. \qquad (37)
\end{aligned}
$$

Observe that, as a consequence of the introduced scaling, at order ϵ^0 the equation ruling the equilibrium configurations of the absorber appears (Eq. 29), whose solutions are $w_0 = 0\ \forall\alpha$ and $w_0 = \pm\sqrt{-1+\alpha^2}$ for $\alpha > 1$. At order ϵ, the linear undamped equation of the prism (Eq. 30) and the linearized equation for the absorber (Eq. 31), which is coupled to that of the prism, appear. Corrections emerge at order ϵ^2 (Eqs. 32–34), where also the equations ruling the electric tension are considered (Eq. 34). From the equations at order ϵ^3, only the first will be used (Eq. 35).

The generating solution of Eq. 30 is:

$$
y_1=\mathcal{A}(t_1,t_2)e^{it_0}+\mathrm{cc}, \qquad (38)
$$

where i is the imaginary unit, cc stands for the complex conjugate and $\mathcal{A}(t_1,t_2)$ is a slow-varying amplitude to be evaluated.

Then, at the same order, Eq. 31 is considered, whose solution is evaluated by the harmonic balance, making:

$$
w_1=\sum_j\mathcal{B}_1^{(j)}(t_1,t_2)e^{ijt_0}+\mathrm{cc}, \qquad (39)
$$

where $\mathcal{B}_1^{(j)}$ are slow-varying amplitudes, still to be evaluated. Substituting Eqs. 38 and 39 into Eq. 31 and balancing terms of frequency 1 (other frequency terms are not considered in this paper) produces:

$$
\begin{aligned}
&\mathcal{A}\beta-\mathcal{B}_1\kappa+\mathcal{B}_1-2i\mathcal{B}_1\zeta_N\\
&\quad-\frac{\alpha\mathcal{B}_1\kappa w_0^2}{\sqrt{w_0^2+1}w_0^2+\sqrt{w_0^2+1}}+\frac{\alpha\mathcal{B}_1\kappa}{\sqrt{w_0^2+1}}=0 \qquad (40)
\end{aligned}
$$

At the next perturbation order, the resonant term on the right-hand side of Eq. 32 is now considered and put to zero, to prevent the existence of secular terms in the solution. This provides the Amplitude Modulation Equation (AME):

$$
\begin{aligned}
d_1\mathcal{A}={}&\frac{35\mathcal{A}^4A_7A_1^5\bar{\mathcal{A}}^3}{4096\zeta_y^5m^{*6}}+\frac{5\mathcal{A}^3A_5A_1^3\bar{\mathcal{A}}^2}{128\zeta_y^3m^{*4}}\\
&+\frac{3\mathcal{A}^2A_3A_1\bar{\mathcal{A}}}{16\zeta_ym^{*2}}+\frac{\mathcal{A}A_1\hat{U}}{4m^*}-\frac{i\mathcal{B}_1\hat{m}}{2\beta} \qquad (41)
\end{aligned}
$$

Taking into account Eq. 41, the solution of Eq. 32 is:

$$
\begin{aligned}
y_2={}&\left(\frac{21iA_1^5A_7}{16384\zeta_y^5m^{*6}}\mathcal{A}^5\bar{\mathcal{A}}^2+\frac{iA_1A_3}{64\zeta_ym^{*2}}\mathcal{A}^3\right.\\
&\left.+\frac{5iA_1^3A_5}{1024\zeta_y^3m^{*4}}\mathcal{A}^4\bar{\mathcal{A}}\right)e^{3it_0}\\
&-\left(\frac{7iA_1^5A_7}{49152\zeta_y^5m^{*6}}\mathcal{A}^6\bar{\mathcal{A}}+\frac{iA_1^3A_5}{3072\zeta_y^3m^{*4}}\mathcal{A}^5\right)e^{5it_0}\\
&+\frac{iA_1^5A_7}{98304\zeta_y^5m^{*6}}\mathcal{A}^7e^{7it_0}+\mathrm{cc}, \qquad (42)
\end{aligned}
$$

and the solution of the Eq. 34 is:

$$
v_2=-\frac{\mathcal{B}_1\sigma_1w_0e^{it_0}}{\sqrt{w_0^2+1}\,(1-i\sigma_2)}+\mathrm{cc}. \qquad (43)
$$

Still at order ϵ^2, the harmonic balance of Eq. 33 is performed, after assuming the solution as:

$$w_2 = \sum_j B_2^{(j)}(t_1, t_2)e^{ijt_0} + cc, \tag{44}$$

and only balancing the harmonic for $j = 1$, to obtain:

$$\begin{aligned}
&-\frac{35i\mathcal{A}^4\beta A_7A_1^5\bar{\mathcal{A}}^3}{2048\zeta_y^5m^{*6}} - \frac{5i\mathcal{A}^3\beta A_5A_1^3\bar{\mathcal{A}}^2}{64\zeta_y^3m^{*4}}\\
&\quad-\frac{3i\mathcal{A}^2\beta A_3A_1\bar{\mathcal{A}}}{8\zeta_ym^{*2}} - \frac{i\mathcal{A}\beta A_1\hat{U}}{2m^*}\\
&\quad-2id_1\mathcal{B}_1 - 2\zeta_Nd_1\mathcal{B}_1 - \mathcal{B}_2\kappa + \mathcal{B}_2 - \mathcal{B}_1\hat{m}\\
&\quad-2i\mathcal{B}_2\zeta_N + \frac{\alpha\mathcal{B}_2\kappa}{\sqrt{w_0^2+1}}\\
&\quad-\frac{\alpha\mathcal{B}_2\kappa w_0^4}{\left(w_0^2+1\right)^{5/2}} - \frac{\alpha\mathcal{B}_2\kappa w_0^2}{\left(w_0^2+1\right)^{5/2}}\\
&\quad-\frac{\mathcal{B}_1\sigma_1w_0^2}{\left(w_0^2+1\right)(1-i\sigma_2)} = 0,
\end{aligned} \tag{45}$$

where $\mathcal{B}_2 = \mathcal{B}_2^{(1)}$. If needed, one can easily obtain the Amplitude Modulation Equation at order ϵ^3 from Eq. 35, which assumes the form:

$$\begin{aligned}
d_2\mathcal{A} = &-\frac{35iA_7A_1^5\mathcal{A}^3\bar{\mathcal{A}}^3d_1\mathcal{A}}{1024\zeta_y^5m^{*6}} + \frac{105iA_7A_1^5\mathcal{A}^4\bar{\mathcal{A}}^2d_1\bar{\mathcal{A}}}{4096\zeta_y^5m^{*6}}\\
&-\frac{15iA_5A_1^3\mathcal{A}^2\bar{\mathcal{A}}^2d_1\mathcal{A}}{128\zeta_y^3m^{*4}}\\
&+\frac{5iA_5A_1^3\mathcal{A}^3\bar{\mathcal{A}}d_1\bar{\mathcal{A}}}{64\zeta_y^3m^{*4}} + \frac{3iA_3A_1\mathcal{A}^2d_1\bar{\mathcal{A}}}{16\zeta_ym^{*2}}\\
&-\frac{3iA_3A_1\mathcal{A}\bar{\mathcal{A}}d_1\mathcal{A}}{8\zeta_ym^{*2}}\\
&-\frac{175\hat{U}A_7A_1^6\mathcal{A}^4\bar{\mathcal{A}}^3}{16384\zeta_y^6m^{*7}} - \frac{15A_5A_1^4\hat{U}\mathcal{A}^3\bar{\mathcal{A}}^2}{512\zeta_y^4m^{*5}}\\
&-\frac{9iA_3^2A_1^2\mathcal{A}^3\bar{\mathcal{A}}^2}{1024\zeta_y^2m^{*4}}\\
&-\frac{3\hat{U}A_3A_1^2\mathcal{A}^2\bar{\mathcal{A}}}{64\zeta_y^2m^{*3}} - \frac{i\hat{U}A_1d_1\mathcal{A}}{4m^*}\\
&+\frac{id_1^2\mathcal{A}}{2} - \frac{\hat{m}d_1\mathcal{B}_1}{\beta} - \frac{i\mathcal{B}_2\hat{m}}{2\beta}
\end{aligned} \tag{46}$$

however, the evaluation of the contributions of w_3 and v_3 is omitted, as the perturbation chain can be conveniently stopped at this step.

After reconstitution, coming back to time τ and considering:

$$\dot{\mathcal{A}} = \epsilon d_1\mathcal{A} + \epsilon^2d_2\mathcal{A}, \quad \mathcal{B} = \epsilon\mathcal{B}_1 + \epsilon^2\mathcal{B}_2, \quad \dot{\mathcal{B}} = \epsilon d_1\mathcal{B}_1, \tag{47}$$

the combinations of Eqs. 41 and 46, and of Eqs. 40 and 45, produce the nonlinear differential system ruling the slow time amplitudes, which reads:

$$\begin{aligned}
\dot{\mathcal{A}} + \frac{3\hat{m}\dot{\mathcal{B}}}{4\beta} = &-\frac{35A_7A_1^5\hat{m}\mathcal{A}^3\mathcal{B}\bar{\mathcal{A}}^3}{4096\beta\zeta_y^5m^{*6}}\\
&-\frac{315A_7A_1^5\hat{m}\mathcal{A}^4\bar{\mathcal{A}}^2\bar{\mathcal{B}}}{16384\beta\zeta_y^5m^{*6}} - \frac{15A_5A_1^3\hat{m}\mathcal{A}^2\mathcal{B}\bar{\mathcal{A}}^2}{512\beta\zeta_y^3m^{*4}}\\
&-\frac{15A_5A_1^3\hat{m}\mathcal{A}^3\bar{\mathcal{A}}\bar{\mathcal{B}}}{256\beta\zeta_y^3m^{*4}} - \frac{3A_3A_1\hat{m}\mathcal{A}\mathcal{B}\bar{\mathcal{A}}}{32\beta\zeta_ym^{*2}}\\
&-\frac{9A_3A_1\hat{m}\mathcal{A}^2\bar{\mathcal{B}}}{64\beta\zeta_ym^{*2}} - \frac{175A_7A_1^6\hat{U}\mathcal{A}^4\bar{\mathcal{A}}^3}{16384\zeta_y^6m^{*7}}\\
&+\frac{35iA_7A_1^6\hat{U}\mathcal{A}^4\bar{\mathcal{A}}^3}{8192\zeta_y^5m^{*7}} + \frac{35A_7A_1^5\mathcal{A}^4\bar{\mathcal{A}}^3}{4096\zeta_y^5m^{*6}}\\
&+\frac{75iA_3A_5A_1^4\mathcal{A}^4\bar{\mathcal{A}}^3}{8192\zeta_y^4m^{*6}}\\
&-\frac{15A_5A_1^4\hat{U}\mathcal{A}^3\bar{\mathcal{A}}^2}{512\zeta_y^4m^{*5}} + \frac{5iA_5A_1^4\hat{U}\mathcal{A}^3\bar{\mathcal{A}}^2}{512\zeta_y^3m^{*5}}\\
&+\frac{5A_5A_1^3\mathcal{A}^3\bar{\mathcal{A}}^2}{128\zeta_y^3m^{*4}} + \frac{9iA_3^2A_1^2\mathcal{A}^3\bar{\mathcal{A}}^2}{1024\zeta_y^2m^{*4}}\\
&-\frac{3A_3A_1^2\hat{U}\mathcal{A}^2\bar{\mathcal{A}}}{64\zeta_y^2m^{*3}} + \frac{3A_3A_1\mathcal{A}^2\bar{\mathcal{A}}}{16\zeta_ym^{*2}} - \frac{iA_1^2\hat{U}^2\mathcal{A}}{32m^{*2}}\\
&+\frac{A_1\hat{U}\mathcal{A}}{4m^*} - \frac{A_1\hat{m}\hat{U}\mathcal{B}}{16\beta m^*} - \frac{i\hat{m}\mathcal{B}}{2\beta},
\end{aligned} \tag{48}$$

$$\begin{aligned}
2(i+\zeta_N)\dot{\mathcal{B}} = &\ \beta\mathcal{A} - \hat{m}\mathcal{B} + \mathcal{B}\\
&-\frac{i\beta A_1\hat{U}\mathcal{A}}{2m^*} - 2i\zeta_N\mathcal{B}\\
&+\kappa\left(-\frac{\alpha w_0^2\mathcal{B}}{\sqrt{w_0^2+1}\,w_0^2+\sqrt{w_0^2+1}} + \frac{\alpha\mathcal{B}}{\sqrt{w_0^2+1}} - \mathcal{B}\right)\\
&-\frac{\sigma_1w_0^2\mathcal{B}}{\left(w_0^2+1\right)(1-i\sigma_2)} - \frac{35i\beta A_7A_1^5\mathcal{A}^4\bar{\mathcal{A}}^3}{2048\zeta_y^5m^{*6}}\\
&-\frac{5i\beta A_5A_1^3\mathcal{A}^3\bar{\mathcal{A}}^2}{64\zeta_y^3m^{*4}} - \frac{3i\beta A_3A_1\mathcal{A}^2\bar{\mathcal{A}}}{8\zeta_ym^{*2}}.
\end{aligned} \tag{49}$$

Real amplitudes and phases are introduced as follows:

$$\mathcal{A}(\tau) = \frac{1}{2} a(\tau) e^{i\gamma(\tau)} + \text{cc}, \qquad \mathcal{B}(\tau) = \frac{1}{2} b(\tau) e^{i\varphi(\tau)} + \text{cc} \tag{50}$$

and are substituted in Eqs. 48–49. Separating real and imaginary parts, combining the phase equations and defining the phase difference as

$$\psi(\tau) = \varphi(\tau) - \gamma(\tau), \tag{51}$$

produce the following set of Reduced Amplitude Modulation Equations (RAME):

$$\dot{a} = \mathcal{F}_1(a, b, \psi), \tag{52}$$

$$\dot{b} = \mathcal{F}_2(a, b, \psi), \tag{53}$$

$$ab\dot{\psi} = \mathcal{F}_3(a, b, \psi), \tag{54}$$

where the function $\mathcal{F}_j(a, b, \psi)$, $j = 1, 2, 3$ are not reported for the sake of brevity.

The equilibrium solutions of Eqs. 52–54 are evaluated after posing $\dot{a} = \dot{b} = \dot{\psi} = 0$ and applying arc-length continuation for modifying U_r [62]. As amplitudes and phases are detected at equilibrium, the reconstruction of the state variables is performed with Eqs. 25, 26, 38, 39, 42, 43, 44.

For the parameter values given in Table 1, analytical solutions y and w as functions of reduced velocity U_r are shown in Fig. 11 for the Pure Galloping case, in Fig. 12 for $\alpha = 0.5$, and in Fig. 13 for $\alpha = 1.5$. In these plots, the analytical results are compared to those from the numerical integration of the dimensionless mathematical model. In all the cases, supercritical bifurcations are found, where for increasing U_r the always existing trivial solution loses stability at bifurcation, and stable limit cycles appear.

More specifically regarding outcomes, the Pure Galloping case (Fig. 11) is very well caught by the analytical solution in the neighborhood of the critical velocity, i.e. up to $U_r \simeq 15$, which is actually about 30% larger than that. After that value, further perturbation steps would be required to obtain better agreement. Consistently, the case $\alpha = 0.5$ shown in Fig. 12, where oscillations of the control device occur around the trivial equilibrium, provides a very good agreement both in the critical velocity and in the limit cycle amplitudes, for y and w, still up to $U_r \simeq 15$. The case $\alpha = 1.5$ is shown in Fig. 13, where oscillations of the control device occur around the non-trivial equilibrium. Here the analytical solution catches the critical condition and the regular part of the solution for y very well, whereas accuracy is lost for y as non-regular responses occur. In turn, $\max\{w\}$ is still caught in good agreement.

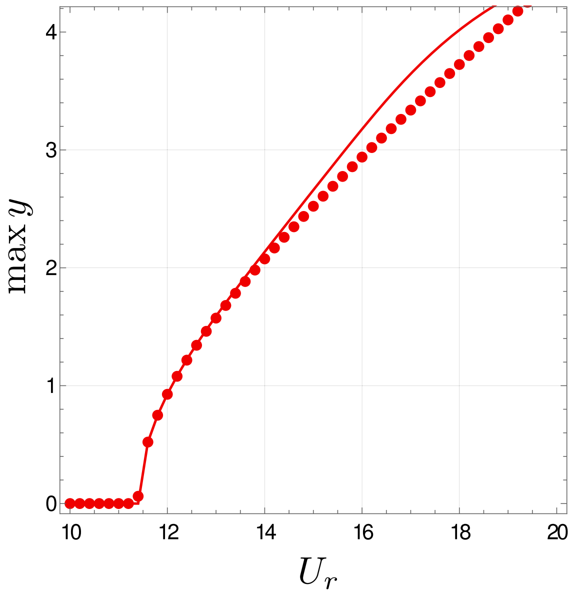

Fig. 11 Analytical (solid line) and numerical (dotted line) max values of the solution for the pure galloping case

5 Conclusions

The paper numerically investigated a device for simultaneous piezoelectric energy harvesting and passive suppression of oscillations. The device is composed of a small mass attached to the main structure (here, a rigid and elastically mounted square prism) by a pre-compressed piezoelectric spring and a linear dashpot. This pre-compression induced two stable equilibrium points, justifying the adopted nomenclature bistable piezoelectric nonlinear energy sink (BSPNES).

Due to the large number of parameters of the mathematical model, focus was placed on three of them, namely the device dashpot, stiffness and pre-compression, represented by the dimensionless quantities ζ_N, κ and α respectively. The analysis of the stability of the equilibrium configuration indicated that, depending on the choice of ζ_N, κ and α, a marked increase in the critical flow velocity may be achieved. The latter condition is positive for passive suppression,

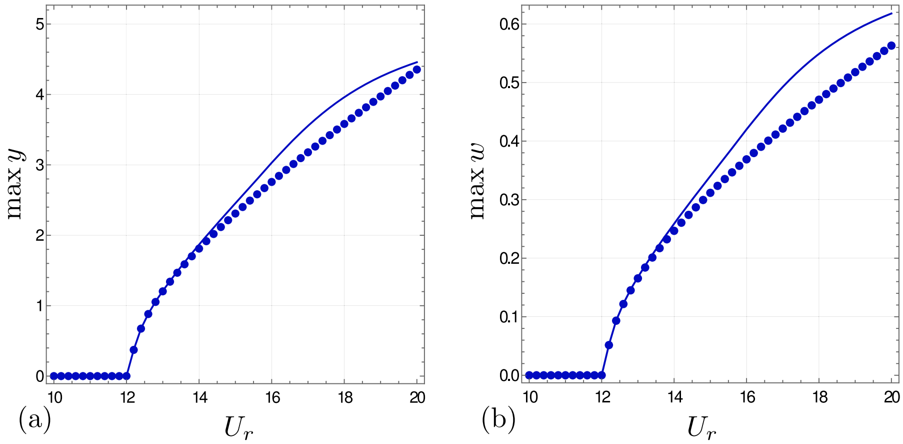

Fig. 12 Analytical (solid line) and numerical (dotted line) max values of the solutions for $\alpha = 0.5$

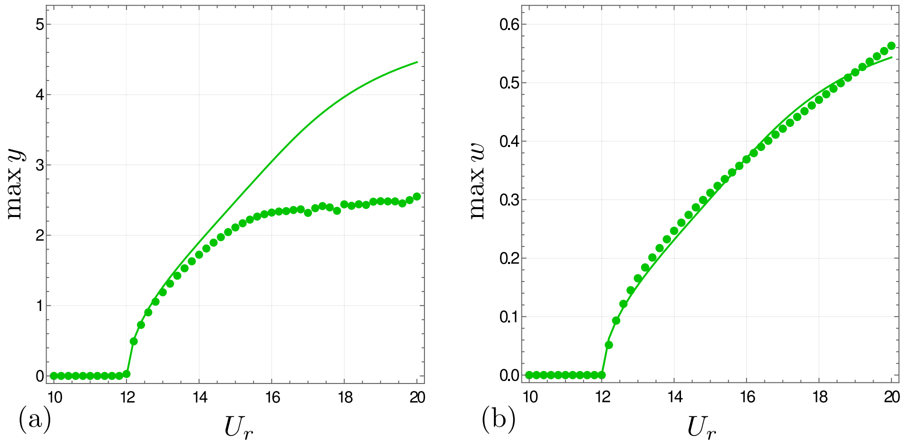

Fig. 13 Analytical (solid line) and numerical (dotted line) max values of the solutions for $\alpha = 1.5$

but not for energy harvesting. In this scenario, the values of ζ_N and κ were chosen such that a slight increase in the critical reduced velocity was achieved.

Once ζ_N and κ were defined, the performance of the device was investigated for a wide range of reduced velocity for two different values of α. Particularly one value of α led to bistability (hence, to the so called BSPNES) and the other ($\alpha = 0.5$) to a monostable system. In terms of passive suppression of oscillations, the performance of the BSPNES was significantly better than that from the monostable for reduced velocities ranging from 15 to 35. In terms of energy harvesting, the BSPNES also exhibited a superior performance when compared to its monostable counterpart. For the BSPNES, the prism showed strongly modulated responses of maximum value much smaller than those from the Pure Galloping case. In addition to the numerical results, analytical studies based on perturbations methods were developed. More specifically, the Multiple Scale-Harmonic Balance Method was used to obtain the Amplitude Modulation Equations, which very well capture the modification of the galloping phenomenon due to the effects of the control device and the harvester.

The results and the mathematical model presented herein may be useful for designing similar devices. Obviously, the designer must carefully choose the parameters that define the device, provided a strong performance as a passive suppressor of the main structure response is not positive for energy harvesting purposes. Notice, however, that the bistability led to intervals of reduced velocity of superior performance in terms of both alleviation of the prism response and energy harvesting. Hence, the inclusions of this kind of nonlinearities, if properly tailored, may be of relevance.

Further works include the development of comprehensive studies for choosing a set of device parameters to achieve an optimized performance. This performance will be quantified using a certain objective function still to be defined. Once the device has its parameters tuned for optimization, experiments will be carried out aiming at validating the concept.

Acknowledgements The first author thanks the Brazilian National Council for Scientific and Technological Development (CNPq) for Grant 305945/2020-3 and the São Paulo Research Foundation (FAPESP) for sponsoring a comprehensive research on passive suppression and energy harvesting from structural oscillations, Grant 2022/02995-9. The second author is grateful to FAPESP for his PhD scholarships (Grants 2021/04434-1 and 2022/12546-7). FAPESP also supports a Thematic Project on nonlinear dynamics applied to engineering systems (Grant 2022/00770-0). Dr. Michael Selwanis is also acknowledged for the discussions regarding the force coefficients.

Author contributions GRF: Conceptualization, Methodology, Software, Formal analysis, Writing, Visualization, Funding acquisition. VSFM: Software, Writing. GJV: Writing, Analytical studies. DZ: Writing, Analytical Studies.

Funding This work was supported by the São Paulo Research Foundation (Grant Numbers 2022/02995-9, 2022/00770-0, 2022/12546-7 and 2021/04434-1). GRF has received research support from the Brazilian National Council for Scientific and Technological Development (Grant 305945/2020-3).

Data availability The codes developed are not public. However, the interested reader can contact the corresponding author for requesting the files.

Declarations

Conflict of interest The authors declare to have no conflict of interest.

Appendix A: A discussion on bistability

The bistable behavior of the BSPNES can be discussed in the light of the simpler problem with one degree of freedom (namely, its vertical position W) sketched in Fig. 14. As well known, the equilibrium position is governed by potential energy $\mathcal{U}$, which is a function of spring stiffness k and stretched and unstretched lengths ℓ and ℓ_0, respectively. Since $\ell = \sqrt{\ell_1^2 + W^2}$ and defining $\Delta\ell = \ell - \ell_0$, the potential energy is given by Eq. 55.

$$\mathcal{U} = \frac{1}{2}k(\Delta\ell)^2 = \frac{1}{2}k\ell_1^2\left(1 + w^2 - 2\alpha\sqrt{1+w^2} + \alpha^2\right) \tag{55}$$

We define dimensionless potential energy $\hat{\mathcal{U}}$ by Eq. 56

$$\hat{\mathcal{U}} = \frac{\mathcal{U}}{\frac{1}{2}k\ell_1^2} = 1 + w^2 - 2\alpha\sqrt{1+w^2} + \alpha^2 \tag{56}$$

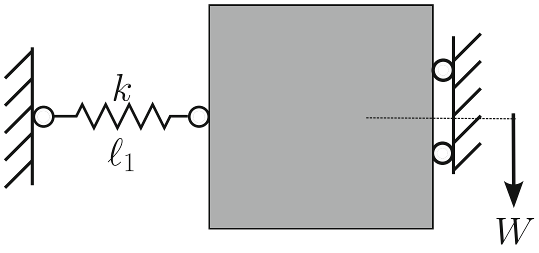

Fig. 14 Schematic representation of the simpler problem. The gravitational effect is not considered

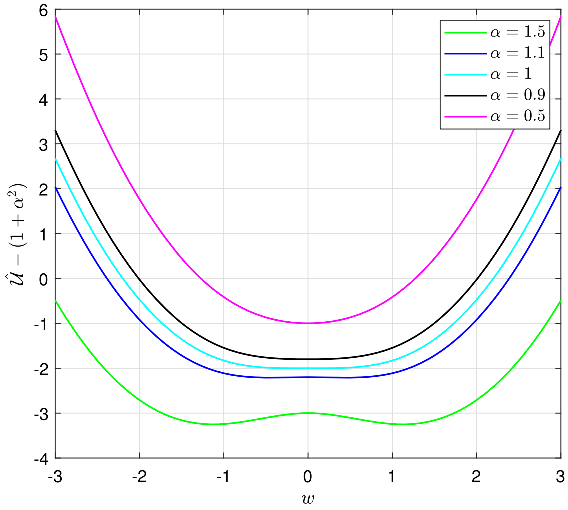

Fig. 15 Variation of $\hat{\mathcal{U}} - (1 + \alpha^2)$ with respect to w

where, as in the main part of the paper, $w = W/\ell_1$ and $\alpha = \ell_0/\ell_1$. For the stability study, the term $1 + \alpha^2$ in Eq. 56 is not relevant, provided it shifts the curve along the vertical axis. Equilibrium points w_0 are obtained from:

$$\left(\frac{d\hat{\mathcal{U}}}{dw}\right)_{w_0} = 0 \Rightarrow w_0\left(1 - \frac{\alpha}{\sqrt{1+w_0^2}}\right) = 0$$
$$\Leftrightarrow w_0 = 0;\ w_0 = \pm\sqrt{\alpha^2 - 1} \tag{57}$$

Local minima of the potential energy correspond to stable equilibrium points, whereas local maxima characterize unstable equilibrium points. Figure 15 depicts the variation of $\hat{\mathcal{U}} - (1+\alpha^2)$ with respect to the dimensionless displacement w for different values of α. From this plot and considering $\alpha > 1$, notice that $w_0 = 0$ is an unstable equilibrium point and $w_0 = \pm\sqrt{\alpha^2 - 1}$ are two stable equilibrium points (bistable system).

Intrawell oscillations are those characterized by oscillations around one of the stable equilibrium points.

In turn, interwell oscillations correspond to oscillations that cover the two stable equilibrium points. Notice also that the increase in α expands the distance between one stable equilibrium point and the unstable one, increasing the energy level for triggering interwell oscillations.

References

1. Blevins, R.D.: Flow-Induced Vibration, 2nd edn. Krieger Publishing Company, Malabar (2001)
2. Naudascher, E., Rockwell, D.: Flow-Induced Vibrations—An Engineering Guide. Dover Publications, New York (2005)
3. Païdoussis, M.P., Price, S.J., de Langre, E.: Fluid–Structure Interactions—Cross-Flow-Induced Instabilities. Cambridge University Press, Cambridge (2011)
4. Hartog, J.P.D.: Mechanical Vibrations. McGraw-Hill, New York (1956)
5. Lee, Y.S., Vakakis, A.F., Bergman, L.A., McFarland, D.M., Kerschen, G., Nucera, F., Tsakirtzis, S., Panagopoulos, P.N.: Passive non-linear targeted energy transfer and its applications to vibration absorption: a review. J Multi-body Dyn (2008). https://doi.org/10.1243/14644193JMBD118
6. Gendelman, O.V., Manevitch, L.I., Vakakis, A.F., Closkey, R.M.: Energy pumping in nonlinear mechanical oscillators: Part I—Dynamics of the underlying Hamiltonian systems. J. Appl. Mech. **68**, 34–41 (2001). https://doi.org/10.1115/1.1345524
7. Vakakis, A.F., Gendelman, O.V.: Energy pumping in nonlinear mechanical oscillators: Part II - resonance capture. J. Appl. Mech. **68**, 42–48 (2001)
8. Vakakis, A.F.: Passive nonlinear targeted energy transfer. Philos. Trans. R. Soc. A **376**, 1–15 (2018). https://doi.org/10.1098/rsta.2017.0132
9. Tumkur, R.K.R., Domany, E., Gendelman, O.V., Masud, A., Bergman, L.A., Vakakis, A.F.: Reduced-order model for laminar vortex-induced vibration of a rigid circular cylinder with an internal nonlinear absorber. Commun. Nonlinear Sci. Numer. Simul. **18**, 1916–1930 (2013). https://doi.org/10.1016/j.cnsns.2012.11.028
10. Mehmood, A., Nayfeh, A.H., Hajj, A.A.: Effects of a nonlinear energy sink (NES) on vortex-induced vibrations of a circular cylinder. Nonlinear Dyn. **77**, 667–680 (2014). https://doi.org/10.1007/s11071-014-1329-x
11. Blanchard, A.B., Gendelman, O.V., Bergman, L.A., Vakakis, A.F.: Capture into a slow-invariant-manifold in the fluid-structure dynamics of a sprung cylinder with a nonlinear rotator. J. Fluids Struct. **63**, 155–173 (2016). https://doi.org/10.1016/j.jfluidstructs.2016.03.009
12. Dai, H.L., Abdelkefi, A., Wang, L.: Vortex-induced vibrations mitigation through a nonlinear energy sink. Commun. Nonlinear Sci. Numer. Simul. **42**, 22–36 (2017). https://doi.org/10.1016/j.cnsns.2016.05.014
13. Dongyang, C., Abbas, L.K., Guoping, W., Xiaoting, R., Marzocca, P.: Numerical study of flow-induced vibrations of cylinders under the action of nonlinear energy sinks (NESs). Nonlinear Dyn. (2018). https://doi.org/10.1007/s11071-018-4402-z
14. Blanchard, A., Bergman, L.A., Vakakis, A.: Vortex-induced vibration of a linearly sprung cylinder with an internal rotational nonlinear energy sink in turbulent flow. Nonlinear Dyn. (2019). https://doi.org/10.1007/s11071-019-04775-3
15. Ueno, T., Franzini, G.R.: Numerical studies on passive suppression of one and two degrees-of-freedom vortex-induced vibrations using a rotative non-linear vibration absorber. Int. J. Non-Linear Mech. **116**, 230–249 (2019). https://doi.org/10.1016/j.ijnonlinmec.2019.07.001
16. Chen, D., Marzocca, P., Xiao, Q., Zhan, Z., Gu, C.: Vortex-induced vibration on a low mass ratio cylinder with a nonlinear dissipative oscillator at moderate Reynolds number. J. Fluids Struct. **99**, 103160 (2020). https://doi.org/10.1016/j.jfluidstructs.2020.103160
17. Franzini, G.R.: An elastic rotative nonlinear vibration absorber (ERNVA) as a passive suppressor for vortex-induced vibrations. Nonlinear Dyn. **103**, 255–277 (2021). https://doi.org/10.1007/s11071-020-06149-6
18. Augusto, J., Silva, I., Marques, F.D.: Multi-degree of freedom nonlinear energy sinks for passive control of vortex-induced vibrations in a sprung cylinder. Acta Mech. (2021). https://doi.org/10.1007/s00707-021-03037-x
19. Dai, H.L., Abdelkefi, A., Wang, L.: Usefulness of passive non-linear energy sinks in controlling galloping vibrations. Int. J. Non-Linear Mech. **81**, 83–94 (2016). https://doi.org/10.1016/j.ijnonlinmec.2016.01.007
20. Teixeira, B., Franzini, G.R., Gosselin, F.P.: Passive suppression of transverse galloping using a non-linear energy sink. In: Proceedings of 9th International Symposium on Fluid-Structure Interactions, Flow-Sound Interactions, Flow-Induced Vibration & Noise (2018)
21. Selwanis, M.M., Franzini, G.R., Béguin, C., Gosselin, F.P.: Wind tunnel demonstration of galloping mitigation with a purely nonlinear energy sink. J. Fluids Struct. **100**, 103169 (2021). https://doi.org/10.1016/j.jfluidstructs.2020.103169
22. Selwanis, M.M., Franzini, G.R., Béguin, C., Gosselin, F.P.: Multi-ball rotative nonlinear energy sink for galloping mitigation. J. Sound Vib. (2022). https://doi.org/10.1016/j.jsv.2022.116744
23. Selwanis, M.M., Franzini, G.R., Béguin, C., Gosselin, F.P.: How a ball free to orbit in a circular track mitigates the galloping of a square prism. Nonlinear Dyn. **111**, 179–197 (2023). https://doi.org/10.1007/s11071-022-07830-8
24. Shirude, A., Vyasarayani, C.P., Chatterjee, A.: Towards design of a nonlinear vibration stabilizer for suppressing single-mode instability. Nonlinear Dyn. **103**, 1563–1583 (2021). https://doi.org/10.1007/s11071-021-06207-7
25. Luongo, A., Zulli, D.: Aeroelastic instability analysis of nes-controlled systems via a mixed multiple scale/harmonic balance method. J. Vib. Control **20**(13), 1985–1998 (2014). https://doi.org/10.1177/1077546313480542
26. Pacheco, D.R.Q., Marques, F.D., Ferreira, A.J.M.: Panel flutter suppression with nonlinear energy sinks: Numerical modeling and analysis. Int. J. Non-Linear Mech. **106**, 108–114 (2018). https://doi.org/10.1016/j.ijnonlinmec.2018.08.009
27. Maciel, V.S.F., Kheiri, M., Franzini, G.R.: Passive suppression of flow-induced vibrations of a cantilevered pipe discharging fluid using non-linear vibration absorbers. Int. J. Non-Linear Mech. (2022). https://doi.org/10.1016/j.ijnonlinmec.2022.104053

28. Zhou, K., Xiong, F.R., Jiang, N.B., Dai, H.L., Yan, H., Wang, L., Ni, Q.: Nonlinear vibration control of a cantilevered fluid-conveying pipe using the idea of nonlinear energy sink. Nonlinear Dyn. **95**, 1435–1456 (2018). https://doi.org/10.1007/s11071-018-4637-8
29. Mamaghani, A.E., Khadem, S.E., Bab, S.: Vibration control of a pipe conveying fluid under external periodic excitation using a nonlinear energy sink. Nonlinear Dyn. **86**, 1761–1795 (2016). https://doi.org/10.1007/s11071-016-2992-x
30. Ding, H., Chen, L.: Designs, analysis, and applications of nonlinear energy sinks. Nonlinear Dyn. (2020). https://doi.org/10.1007/s11071-020-05724-1
31. Saeed, A.S., Nasar, R.A., AL-Shudeifat, M.A.: A review on nonlinear energy sinks: designs, analysis and applications of impact and rotary types. Nonlinear Dyn. (2022). https://doi.org/10.1007/s11071-022-08094-y
32. Gendelman, O.V., Sigalov, G., Manevitch, L.I., Mane, M., Vakakis, A.F., Bergman, L.A.: Dynamics of an eccentric rotational nonlinear energy sink. J. Appl. Mech. **79**, 110121–110129 (2012). https://doi.org/10.1115/1.4005402
33. Ding, K., Pearlstein, A.: Free response of a rotational nonlinear energy sink coupled to a linear oscillator: Fractality, riddling, and initial-condition sensitivity at intermediate initial displacements. J. Appl. Mech. **88**, 121009 (2021). https://doi.org/10.1115/1.4051998
34. Gendelman, O.V., Alloni, A.: Dynamics of forced system with vibro-impact energy sink. J. Sound Vib. **358**, 301–314 (2015). https://doi.org/10.1016/j.jsv.2015.08.020
35. Al-Shudeifat, M.A., Saeed, A.S.: Comparison of a modified vibro-impact nonlinear energy sink with other kinds of NESs. Meccanica (2020). https://doi.org/10.1007/s11012-020-01193-3
36. Feudo, S.L., Job, S., Cavallo, M., Fraddosio, A., Piccioni, M.D., Tafuni, A.: Finite contact duration modeling of a vibro-impact nonlinear energy sink to protect a civil engineering frame structure against seismic events. Eng. Struct. (2022). https://doi.org/10.1016/j.engstruct.2022.114137
37. Al-Shudeifat, M.A.: Highly efficient nonlinear energy sink. Nonlinear Dyn. **76**, 1905–1920 (2014). https://doi.org/10.1007/s11071-014-1256-x
38. Chen, Y.Y., Qian, Z.C., Zhao, W., Chang, C.M.: A magnetic bi-stable nonlinear energy sink for structural seismic control. J. Sound Vib. (2020). https://doi.org/10.1016/j.jsv.2020.115233
39. Li, H., Li, A., Kong, X.: Design criteria of bistable nonlinear energy sink in steady-state dynamics of beams and plates. Nonlinear Dyn. (2021). https://doi.org/10.1007/s11071-020-06178-1
40. Chen, Y., Su, W., Tesfamariam, S., Qian, Z., Zhao, W., Yang, Z., Zhou, F.: Experimental study of magnetic bistable nonlinear energy sink for structural seismic control. Soil Dyn. Earthq. Eng. (2023). https://doi.org/10.1016/j.soildyn.2022.107572
41. Erturk, A., Inman, D.J.: Piezoelectric Energy Harvesting. Wiley, New Jersey (2011)
42. Bernitsas, M.M., Raghavan, K., Ben-Simon, Y., Garcia, E.M.H.: VIVACE (vortex induced vibration aquatic clean energy): a new concept in generation of clean and renewable energy from fluid flow. J. Offshore Mech. Arct. Eng. **130**, 1–19 (2008). https://doi.org/10.1115/1.2957913
43. Barrero-Gil, A., Alonso, G., Sanz-Andres, A.: Energy harvesting from transverse galloping. J. Sound Vib. **329**, 2873–2883 (2010). https://doi.org/10.1016/j.jsv.2010.01.028
44. Mehmood, A., Abdelkefi, A., Hajj, A.A., Nayfeh, A.H., Akthar, I., Nuhait, A.O.: Piezoelectric energy harvesting from vortex-induced vibrations of circular cylinder. J. Sound Vib. **332**, 4656–4667 (2013). https://doi.org/10.1016/j.jsv.2013.03.033
45. Dai, H.L., Abdelkefi, A., Wang, L.: Piezoelectric energy harvesting from concurrent vortex-induced vibrations and base excitations. Nonlinear Dyn. **77**, 967–981 (2014). https://doi.org/10.1007/s11071-014-1355-8
46. Grouthier, C., Michelin, S., Bourguet, R., Modarres-Sadeghi, Y., de Langre, E.: On the efficiency of energy harvesting using vortex-induced vibrations of cables. J. Fluids Struct. **49**, 427–440 (2014). https://doi.org/10.1016/j.jfluidstructs.2014.05.004
47. Dai, H.L., Abdelkefi, A., Javed, U., Wang, L.: Modeling and performance of electromagnetic energy harvesting from galloping oscillations. Smart Mater. Struct. (2015). https://doi.org/10.1088/0964-1726/24/4/045012
48. Antoine, G.O., de Langre, E., Michelin, S.: Optimal energy harvesting from vortex-induced vibrations of cables. Philos. Trans. R. Soc. A **472**, 1–18 (2016). https://doi.org/10.1098/rspa.2016.0583
49. Hémon, P., Amandolese, X., Andrianne, T.: Energy harvesting from galloping of prisms: a wind tunnel experiment. J. Fluids Struct. **70**, 390–402 (2017). https://doi.org/10.1016/j.jfluidstructs.2017.02.006
50. Franzini, G.R., Bunzel, L.O.: A numerical investigation on piezoelectric energy harvesting from vortex-induced vibrations with one and two degrees of freedom. J. Fluids Struct. **77**, 196–212 (2018). https://doi.org/10.1016/j.jfluidstructs.2017.12.007
51. Madi, L.S., Vernizzi, G.J., Pesce, C.P.: 3d reduced order model for an orthotropic stiffened piezoelectric cantilevered flexible cylinder under VIV. In: Proceedings of the 2nd International Nonlinear Dynamics Conference—NODYCON2021 (2021)
52. Abdelkefi, A.: Aeroelastic energy harvesting: a review. Int. J. Eng. Sci. **100**, 112–135 (2016). https://doi.org/10.1016/j.ijengsci.2015.10.006
53. Wang, J., Yurchenko, D., Hu, G., Zhao, L., Tang, L., Yang, Y.: Perspectives in flow-induced vibration energy harvesting. Appl. Phys. Lett. (2021). https://doi.org/10.1063/5.0063488
54. Paula, A.S.D., Inman, D.J., Savi, M.A.: Energy harvesting in a nonlinear piezomagnetoelastic beam subjected to random excitation. Mech. Syst. Signal Process. **54**, 405–416 (2015). https://doi.org/10.1016/j.ymssp.2014.08.020
55. Kremer, D., Liu, K.: A nonlinear energy sink with an energy harvester: transient responses. J. Sound Vib. **333**, 4859–4880 (2014). https://doi.org/10.1016/j.jsv.2014.05.010
56. Araujo, G.P., da Silva, J.A.I., Marques, F.D.: Energy harvesting from a rotational nonlinear energy sink in vortex-induced vibrations. J. Fluids Struct. **113**, 103656 (2022). https://doi.org/10.1016/j.jfluidstructs.2022.103656
57. Lossouarn, B., Deü, J.F., Aucejo, M.: Multimodal vibration damping of a beam with a periodic array of piezoelectric patches connected to a passive electrical network.

Smart Mater. Struct. **24**, 1–14 (2015). https://doi.org/10.1088/0964-1726/24/11/115037
58. Rackauckas, C., Nie, Q.: Differentialequations.jl—a performant and feature-rich ecosystem for solving differential equations in Julia. J. Open Res. Softw. **5**(1) (2017)
59. Luongo, A., Zulli, D.: Dynamic analysis of externally excited NES-controlled systems via a mixed Multiple Scale/Harmonic Balance algorithm. Nonlinear Dyn. **70**(3), 2049–2061 (2012)
60. Luongo, A., Casciati, S., Zulli, D.: Perturbation method for the dynamic analysis of a bistable oscillator under slow harmonic excitation. Smart Struct. Syst. **18**(1), 183–196 (2016)
61. Settimi, V., Rega, G.: Asymptotic formulation of the nonlinear bifurcation scenarios in thermomechanically coupled plates. Nonlinear Dyn. **111**, 5941–5962 (2023)
62. Doedel, E.J., Olderman, B.E.: AUTO-07P: Continuation and Bifurcation Software for Ordinary Differential Equation (2021). http://cmvl.cs.concordia.ca/auto/